



















The SPIRou legacy survey

Rotation period of quiet M dwarfs from circular polarization in near-infrared spectral lines: I. The SPIRou APERO analysis

P. Fouqué¹ *, E. Martioli^{2,3} , J.-F. Donati¹ , L.T. Lehmann¹ , B. Zaire^{1,4} , S. Bellotti^{1,5} , E. Gaidos⁶ , J. Morin⁷, C. Moutou¹ , P. Petit¹ , S.H.P. Alencar⁴, L. Arnold⁸ , É. Artigau⁹ , T.-Q. Cang¹⁰, A. Carmona¹¹ , N.J. Cook⁹ , P. Cortés-Zuleta¹² , P.I. Cristofari¹, X. Delfosse¹¹ , R. Doyon⁹ , G. Hébrard³ , L. Malo⁹, C. Reylé¹³ ,
and C. Usher⁸

¹ Institut de Recherche en Astrophysique et Planétologie, Université de Toulouse, CNRS, 14 avenue Edouard Belin, F-31400, Toulouse, France, e-mail: Pascal.Fouque@irap.omp.eu

² Laboratório Nacional de Astrofísica, Rua Estados Unidos 154, 37504-364, Itajubá - MG, Brazil

³ Institut d'Astrophysique de Paris, CNRS, Sorbonne Université, 98 bis bd Arago, 75014 Paris, France

⁴ Departamento de Física-Icex-UFMG Antônio Carlos, 6627, 31270-901 Belo Horizonte, MG, Brazil

⁵ Science Division, Directorate of Science, European Space Research and Technology Centre (ESA/ESTEC), Keplerlaan 1, 2201 AZ, Noordwijk, The Netherlands

⁶ Department of Earth Sciences, University of Hawai'i at Mānoa, 1680 East-West Road, Honolulu, HI, 96822, USA

⁷ Laboratoire Univers et Particules de Montpellier, Université de Montpellier, CNRS, F-34095 Montpellier, France

⁸ Canada-France-Hawaii Telescope, CNRS, Kamuela, HI 96743, USA

⁹ Université de Montréal, Département de Physique, IREX, Montréal, QC H3C 3J7, Canada

¹⁰ Beijing Normal University, No.19, Xijiekouwai St, Haidian District, Beijing, 100875, People's Republic of China

¹¹ Université Grenoble Alpes, CNRS, IPAG, F-38000 Grenoble, France

¹² Laboratoire d'Astrophysique de Marseille, Aix-Marseille Université, CNRS, 38 rue Frédéric Joliot-Curie, F-13388, Marseille, France

¹³ Institut UTINAM, CNRS, Université Bourgogne Franche-Comté, OSU THETA Franche-Comté-Bourgogne, Observatoire de Besançon, BP 1615, 25010 Besançon Cedex, France

Received ; accepted

ABSTRACT

Context. The rotation period of stars is an important parameter together with mass, radius, and effective temperature. It is an essential parameter for any radial velocity monitoring, as stellar activity can mimic the presence of a planet at the stellar rotation period. Several methods exist to measure it, including long sequences of photometric measurements or temporal series of stellar activity indicators.

Aims. Here, we use the circular polarization in near-infrared spectral lines for a sample of 43 quiet M dwarfs and compare the measured rotation periods to those obtained with other methods.

Methods. From Stokes V spectropolarimetric sequences observed with SPIRou at the Canada-France-Hawaii Telescope and the data processed with the APERO pipeline, we computed the least-squares deconvolution profiles using different masks of atomic stellar lines with known Landé factor appropriate to the effective temperature of the star. We derived the longitudinal magnetic field to examine its possible variation in 50 to 200 observations of each star. To determine the stellar rotation period, we applied a Gaussian process regression, enabling us to determine the rotation period of stars with evolving longitudinal field.

Results. We were able to measure a rotation period for 27 of the 43 stars of our sample. The rotation period was previously unknown for 8 of these stars. Our rotation periods agree well with periods found in the literature based on photometry and activity indicators, and we confirm that near-infrared spectropolarimetry is an important tool for measuring rotation periods, even for magnetically quiet stars. Furthermore, we computed the ages for 20 stars of our sample using gyrochronology.

Key words. stars: planetary systems – stars: individual – techniques: polarimetry, radial velocity

1. Introduction

The rotation period (hereafter P_{rot}) is an important characteristic of a star, as is its effective temperature (T_{eff}), mass, radius and corresponding gravity ($\log g$), metallicity ($[M/H]$), and age. In the context of exoplanet search by velocimetry (measure of the radial velocity, RV), the knowledge of the stellar rotation period avoids attributing a periodogram peak to an exoplanet orbital period by taking the systematic noise that is introduced by stellar activity into account (e.g., Queloz et al. 2001). Sev-

* Based on observations obtained at the Canada-France-Hawaii Telescope (CFHT) which is operated from the summit of Maunakea by the National Research Council of Canada, the Institut National des Sciences de l'Univers of the Centre National de la Recherche Scientifique of France, and the University of Hawaii. Based on observations obtained with SPIRou, an international project led by Institut de Recherche en Astrophysique et Planétologie, Toulouse, France.

eral publications identified a periodic signal as due to activity and/or proposed methods to distinguish RV jitter from Keplerian variation (see, e.g., Bonfils et al. 2007; Figueira et al. 2010; Boisse et al. 2011) or identified a signal that was previously announced as due to a planet as actually being caused by activity (e.g., Huélamo et al. 2008; Robertson et al. 2014; Robertson & Mahadevan 2014; Kane et al. 2016; Faria et al. 2020).

Stellar rotation periods for magnetic stars have been measured using the small-scale surface magnetic field, which is detected through the broadening and intensification of some stellar lines due to the Zeeman effect (e.g., Babcock 1947) or the large-scale surface magnetic field derived from the polarimetric signal of spectral lines, as pioneered by Preston (1971); Landstreet (1980) for early-type stars. A periodic variation in the longitudinal magnetic field is interpreted as due to the periodic appearance of magnetic regions at the surface of the star, which allows measuring its rotation period; see Landstreet (1992) for a review. An application to M dwarfs can be found in Donati et al. (2008); Morin et al. (2008, 2010); Hébrard et al. (2016).

Rotation periods can also be measured from long photometric sequences obtained with small telescopes such as ASAS¹ (Pojmanski 1997), APT² (Henry 1999), HATNet³ (Bakos et al. 2004), NSVS⁴ (Woźniak et al. 2004), SuperWASP⁵ (Pollacco et al. 2006), and MEarth (Nutzman & Charbonneau 2008; Irwin et al. 2009); examples can be found in Kiraga & Stepien (2007); Irwin et al. (2011); Suárez Mascareño et al. (2016); Díez Alonso et al. (2019), among others, or more recently, from space telescopes such as Kepler, K2, or TESS⁶ (Díez Alonso et al. 2019).

An alternative technique uses sequences of stellar activity indicators such as H α , Ca II H&K, the Ca II infrared triplet, or values computed at the same time as the radial velocities using the cross-correlation function (CCF) such as the full width at half maximum (FWHM), contrast, or the bisector (e.g., Noyes et al. 1984; Queloz et al. 2001; Bonfils et al. 2007; West et al. 2008; Boisse et al. 2011; Bonfils et al. 2013; Suárez Mascareño et al. 2015; Nelson et al. 2016; Suárez Mascareño et al. 2018; Toledo-Adrón et al. 2019; Lafarga et al. 2021).

In the framework of the SPIRou legacy survey (hereafter SLS), a sample of about 50 nearby low-mass stars is regularly monitored to detect exoplanets using the SPIRou spectropolarimeter (Donati et al. 2020). Some of these targets lack a measured rotation period, and some have several measurements that sometimes disagree. To clarify the situation and increase the sample of known rotation periods, we focus in this paper on determining the rotation period by exploiting the large-scale magnetic field information extracted from the Stokes V profiles of spectral lines.

The paper is organized as follows: Section 2 briefly describes SPIRou⁷ and the SPIRou Legacy Survey (SLS⁸; id P40 and P42, PI: Jean-François Donati). Section 3 describes the generic software called *A PipelinE to Reduce Observations* APERO⁹ (v0.7.232, Cook et al. 2022), which is used to reduce the SPIRou observations, in particular, the spectropolarimetric analysis and

the derivation of the longitudinal magnetic field. Section 4 explains the results for the stars in our sample, separating them into three categories according to their spectral type. Two examples are treated in detail, and a comparison is made with results from the literature. Finally, Section 5 examines our general results and further perspectives.

2. Observations

Observations are part of the CFHT large program SPIRou Legacy Survey. SPIRou is a stabilized high-resolution near-infrared (NIR) spectropolarimeter (Donati et al. 2020) mounted on the 3.6 m CFHT at the top of Maunakea, Hawaii. It is designed for high-precision velocimetry and spectropolarimetry to detect and characterize exoplanets and stellar magnetic fields. It provides full coverage of the NIR spectrum from 950 nm to 2500 nm at a spectral resolving power of $\lambda/\Delta\lambda \sim 70\,000$.

The SLS was allocated 310 nights over seven semesters (February 2019 to June 2022). It covers three different science topics, called work packages (see Donati et al. 2020 for details). The analysis of this paper is restricted to work package 1 (WP1), dedicated to a blind planet search. More than 50 M dwarfs were regularly monitored during the SPIRou runs (typically ten contiguous nights per month). We excluded monitored active stars with short and well-known rotation periods from this study ($P_{\text{rot}} < 5$ d): G1388 (AD Leo), G1406 (CN Leo), G1873 (EV Lac), GJ 1111 (DX Cnc), GJ 1154, GJ 1245B, GJ 3622, and PM J18482+0741. We therefore selected 43 stars in the original WP1 sample for which about 150 (50 at least, 250 at most) polarimetric sequences (of four individual subexposures each) have been secured. This represents about 6800 visits, corresponding to more than 27 000 individual spectra secured for the considered sample. The stars belonging to our sample and their stellar characteristics are given in Table 1: *Gaia* absolute magnitudes and colors use *Gaia* DR3 *Gaia* Collaboration et al. (2021); effective temperatures and metallicities come from Cristofari et al. (2022), who used the same set of observations and the same sample (except for G1581, which does not satisfy our criterion of the minimum number of visits); and masses were computed from absolute 2MASS K_s magnitude and metallicity using the Mann et al. 2019 relations. The relative precision of these masses is 2–3% according to Mann et al. (2019), and the internal errors amount to 30 K and 0.1 dex for T_{eff} and $[M/H]$, according to Cristofari et al. (2022). We divided our sample into three subsamples according to a proxy of stellar mass. These three mass bins correspond to the three types of magnetic behavior identified among active M dwarfs by Morin et al. (2010) (see Figure 15 therein). We prefer to define regions according to the absolute G magnitude rather than using the spectral types. Although they match on average, a low metallicity makes the star fainter at a given spectral type: G1412A (M1.0V, $[M/H] = -0.42$) is 1 mag fainter in G than G1410 (M1V, $[M/H] = +0.05$), therefore both should not belong to the same group. The horizontal lines in Table 1 separate the three subsamples. The number of visits corresponds to the initial number, before some polarimetric sequences were rejected for the reasons explained in Sec. 3.2. Finally, we list the FWHM of the median Stokes I profile of each star because it was used to define the velocity range on which we measured the longitudinal magnetic field from the Stokes V profile, as explained in Sec. 3.2.

¹ All Sky Automated Survey

² Automatic Photoelectric Telescope

³ Hungarian-made Automated Telescope Network

⁴ Northern Sky Variability Survey

⁵ Wide Angle Search for Planets

⁶ Transiting Exoplanet Survey Satellite

⁷ <http://spirou.irap.omp.eu> and <https://www.cfht.hawaii.edu/Instruments/SPIRou/>

⁸ <http://spirou.irap.omp.eu/Observations/The-SPIRou-Legacy-Survey>

⁹ <https://github.com/njcuk9999/aperodrs>

Table 1. Stellar characteristics of the sample of 43 M dwarfs. For uncertainties on mass, T_{eff} , and $[M/H]$, see text. The three sections correspond to early-, mid-, and late-type M dwarfs from top to bottom

Star Units	spectral type	M_G mag	$G_{\text{BP}} - G_{\text{RP}}$ mag	mass M_{\odot}	T_{eff} K	$[M/H]$ dex	visits	FWHM Stokes I km s^{-1}
G1338B	M0V	8.046	1.846	0.58	3952	-0.08	58	6.95 ± 0.25
G1846	M0.5V	8.282	1.967	0.57	3833	0.07	194	6.65 ± 0.26
G1205	M1.5V	8.327	2.122	0.58	3771	0.43	160	6.54 ± 0.16
G1410	M1V	8.426	2.006	0.55	3842	0.05	131	7.73 ± 0.21
G1880	M1.5V	8.611	2.151	0.55	3702	0.26	166	6.37 ± 0.17
G1514	M1.0V	8.793	2.088	0.50	3699	-0.07	177	5.84 ± 0.29
G1382	M2.0V	8.898	2.234	0.51	3644	0.15	124	6.34 ± 0.31
G1752A	M3.0V	9.240	2.379	0.47	3558	0.11	130	6.06 ± 0.23
G148	M2.5V	9.364	2.459	0.46	3529	0.08	194	5.99 ± 0.26
G1617B	M3V	9.459	2.483	0.45	3525	0.20	149	6.09 ± 0.21
G1412A	M1.0V	9.460	2.104	0.39	3620	-0.42	224	5.50 ± 0.24
G115A	M1.5V	9.460	2.164	0.39	3611	-0.33	256	5.76 ± 0.26
G1849	M3V	9.511	2.542	0.46	3502	0.35	203	6.17 ± 0.22
G1411	M2.0V	9.522	2.216	0.39	3589	-0.38	182	4.93 ± 0.18
G1480	M3.5V	9.565	2.591	0.45	3509	0.26	104	6.14 ± 0.22
G1436	M3.0V	9.631	2.449	0.42	3508	0.03	90	5.89 ± 0.33
G1687	M3.0V	9.739	2.518	0.39	3475	0.01	227	5.69 ± 0.20
G1408	M2.5V	9.831	2.430	0.38	3487	-0.09	179	6.17 ± 0.33
G1317	M3.5V	9.859	2.664	0.42	3421	0.23	79	5.39 ± 0.21
GJ4063	M3.5V	9.982	2.770		3419	0.42	220	5.96 ± 0.22
G1725A	M3.0V	10.119	2.461	0.33	3470	-0.26	219	5.43 ± 0.22
G1251	M3.0V	10.129	2.561	0.35	3420	-0.01	187	5.73 ± 0.26
GJ4333	M3.5V	10.233	2.818	0.37	3362	0.25	193	5.70 ± 0.16
GJ1012	M4V	10.268	2.710	0.35	3363	0.07	142	5.26 ± 0.17
GJ1148	M4V	10.370	2.778	0.34	3354	0.11	105	5.45 ± 0.16
G1876	M3.5V	10.527	2.809	0.33	3366	0.15	88	5.65 ± 0.28
PM J09553-2715	M3V	10.629	2.667	0.29	3366	-0.03	75	5.77 ± 0.25
PM J08402+3127	M3.5V	10.739	2.703	0.28	3347	-0.08	142	5.33 ± 0.25
G1725B	M3.5V	10.790	2.625	0.25	3379	-0.28	212	5.34 ± 0.22
GJ1105	M4V	10.931	2.792	0.27	3324	-0.04	171	5.44 ± 0.17
G1445	M3.5V	10.948	2.702	0.24	3356	-0.24	94	5.21 ± 0.19
GJ3378	M3.5V	10.975	2.791	0.26	3326	-0.05	177	5.65 ± 0.22
G1169.1A	M4V	10.994	2.896	0.28	3307	0.13	185	5.66 ± 0.28
GJ1289	M3.5V	11.556	3.011	0.21	3238	0.05	209	7.60 ± 0.37
PM J21463+3813	M4V	11.591	2.814	0.18	3305	-0.38	187	5.21 ± 0.26
GJ1103	M4.5V	11.817	3.116	0.19	3170	-0.03	70	5.44 ± 0.28
G1699	M4.0V	11.884	2.834	0.16	3311	-0.37	249	6.04 ± 0.32
G115B	M3.5V	11.928	2.836	0.16	3272	-0.42	189	6.33 ± 0.37
G1447	M4.0V	11.960	3.033	0.18	3198	-0.13	60	6.24 ± 0.24
GJ1151	M4.5V	12.158	3.142	0.17	3178	-0.16	157	6.42 ± 0.37
G1905	M5.5V	12.881	3.529	0.15	3069	0.05	220	6.13 ± 0.29
GJ1286	M5.5V	13.344	3.706	0.12	2961	-0.23	113	7.46 ± 0.46
GJ1002	M5.5V	13.347	3.675	0.12	2980	-0.33	146	6.92 ± 0.34

3. SPIRou data reduction and analysis

3.1. APERO reduction

Our SPIRou data were reduced with the software APERO. APERO first performs some initial preprocessing of the 4096×4096 pixel images of the HAWAII 4RGTM (H4RG), applying a series of procedures to correct detector effects, remove background thermal noise, and identify bad pixels and cosmic-ray impacts.

It then uses exposures of a quartz halogen lamp (flat) to calculate the position of 49 of the 50 échelle spectral orders recorded on the detector. It optimally extracts (Horne 1986) spectra of the two science channels (fibers A and B) and the simultaneous reference channel (fiber C). This APERO extraction takes the non-Gaussian shape of the instrument profile generated by the pupil slicer into account. APERO corrects the spectra for the blaze signature of the échelle orders obtained from the flat-field exposures, as described in Cook et al. (2022). Both a 2D

order-by-order and 1 D order-merged spectrum are produced for each channel of each scientific exposure.

The pixel-to-wavelength calibration is obtained from exposures of both a uranium-neon hollow cathode lamp and a Fabry-Pérot etalon, generally following the procedure given in Hobson et al. (2021), but with differences described in Cook et al. (2022). We refer to Sections 5.4 and 6.6 of the latter paper for details about the use of a reference night for the whole survey and updates for each survey night, with subtle differences in the wavelength calibration of fibers AB with respect to fibers A and B separately. This procedure provides wavelengths in the rest frame of the observatory, but APERO also calculates the barycentric Earth radial velocity (BERV) and the barycentric Julian date (BJD) of each exposure using the code `barycorrpy`¹⁰ (Wright & Eastman 2014; Kanodia & Wright 2018). These can then be used to reference the wavelength and time to the barycentric frame of the Solar System.

APERO calculates the spectrum of the telluric transmission using a novel technique based on a model obtained from the collection of standard star observations carried out since the beginning of SPIRou operations in 2019 and a fit made for each individual observation using a revised technique based on the principles explained in Artigau et al. (2014), as briefly described in Cook et al. (2022) and in more details in Artigau et al. (2022). APERO also calculates the Stokes parameters describing the polarization state, as defined, for instance, in Landi Degl'Innocenti (1992). Each orthogonal polarization state is recorded on one science fiber. Four sub-exposures are taken with different positions of the quarter-wave rhombs: the method is described in Donati et al. (1997). The two polarization states of each subexposure are combined to define the Stokes parameters, as explained in Sec. 10.1 of Cook et al. (2022) using equations defined in Bagnulo et al. (2009): the Stokes I parameter measures the intensity, the Stokes V parameter measures the circular polarization, and the Stokes Q and U measure the linear polarization (not used in this work). Another combination defines a null measurement to quantify the quality of the Stokes V detection. The continuum for Stokes I and V can be modeled by an iterative sigma-clip algorithm to fit a polynomial to the data. The spectra are normalized to this continuum before an LSD analysis is performed. More details are given in Martioli et al. (2020); Cook et al. (2022).

3.2. Spectropolarimetry analysis

We further analyzed the SPIRou polarized spectra using the code `spirou-polarimetry`¹¹, which we applied to the telluric-corrected 2D spectra. We assumed that the APERO telluric correction is good enough so that we did not need to exclude zones of telluric water bands in this code. The Stokes I , Stokes V , and null-polarization spectra were compressed to one-line profiles using the least-squares deconvolution (LSD) method of Donati et al. (1997). The line masks used in our LSD analysis were computed using the VALD3 catalog (Piskunov et al. 1995; Ryabchikova et al. 2015) and a MARCS model atmosphere (Gustafsson et al. 2008) with a grid of effective temperatures between 3000 K and 4000 K by steps of 500 K, a constant surface gravity of $\log g = 5.0$ dex, and a micro-turbulent velocity v_{mic} of 1 km s^{-1} . We selected all lines deeper than 3% and with a Landé factor of $g_{\text{eff}} > 0$ for a total of 2460, 1335, and 956 atomic lines for 4000 K, 3500 K, and 3000 K, respectively.

¹⁰ <https://github.com/shbhuk/barycorrpy>

¹¹ <https://github.com/edermartioli/spirou-polarimetry>

We normalized the Stokes V profile using a mean wavelength, a mean depth, and a mean Landé factor of the lines in the mask, but we only used the mean depth to normalize the Stokes I profile. For the 4000 K mask (3500 K and 3000 K), the mean values are 1651.2 nm (1617.9 nm and 1604.8 nm) for the wavelengths, 0.135 (0.133 and 0.155) for the depths, and 1.249 (1.242 and 1.235) for the Landé factors. To ensure that Stokes I LSD profiles have a continuum at 1, we used a linear regression of a significant number of bins located well outside of the line for each profile to improve the continuum normalization. We measured the standard deviation of the values in these bins and rejected the profiles for which this standard deviation significantly deviated from the average over all the profiles. This linear regression gives us a better defined Voigt profile, allowing a more precise measure of the FWHM of the median Stokes I LSD profile of each star.

Not all polarimetric sequences led to a useful measurement of the longitudinal magnetic field. There are several steps of data rejection: the telluric correction of some spectra may fail, some LSD profiles are noisy enough that they cannot be fit by a Voigt profile, and others can be fit, but present a noisier continuum than the rest (see above) and are thus rejected. We only rejected data that might contaminate our results, especially, to build a clean median Stokes I profile on which we measured the FWHM and defined the velocity limits to integrate the Stokes V profile (using 6 FWHM as the measuring window, meaning ± 3 FWHM, generally about $\pm 20 \text{ km s}^{-1}$). The final number of polarimetric sequences used in our study is about 6500, compared to the 6800 initially available sequences for our sample of stars. This is an acceptable loss of about 4% that generally corresponds to spectra with a low signal-to-noise ratio (S/N).

As an example, we took the LSD profiles of the early-M dwarf Gl 410 (DS Leo), which displays mild signs of magnetic activity. Fig. 1 shows the resulting LSD profiles at each observing epoch, stacked vertically. Dynamical maps from left to right correspond to the intensity (Stokes I), the circular polarization (Stokes V), and the null LSD profiles. A nonzero Stokes V profile indicates the presence of magnetic fields, while the null profile allows us to assess the reliability of the Stokes V detection. Finally, Fig. 2 shows the median profile of our time series, where the Zeeman signature is clearly visible in the detection of the Stokes V profile. We also display a median null profile to assess that the Stokes V signature is reliably detected. For comparison, we display the Stokes I , V and null dynamical maps (Fig. 3) and median profiles (Fig. 4) of the late-M dwarf Gl 905, whose longitudinal magnetic field has a similar amplitude as Gl 410. Here again, the Stokes V signal is clearly detected, with a shape corresponding at first order to the first derivative of the Stokes I profile.

In the appendix, we display the Stokes V temporal evolution for each star of our sample. The Stokes I temporal evolution and the median Stokes profiles carry less important information for the present work, and the null profiles are very similar to each other. We decided not to publish them for brevity.

To confirm the consistency of our measurements, we also obtained an independent polarimetric reduction and LSD analysis of our SPIRou data using the pipeline `Libre-Esprit` (Donati et al. 1997, 2020). The results of this alternative analysis will be given in a forthcoming paper (Donati et al., in prep).

3.3. Longitudinal magnetic fields

To diagnose the magnetic field in our sample of stars, we calculated the longitudinal magnetic field B_{ℓ} in the LSD profiles

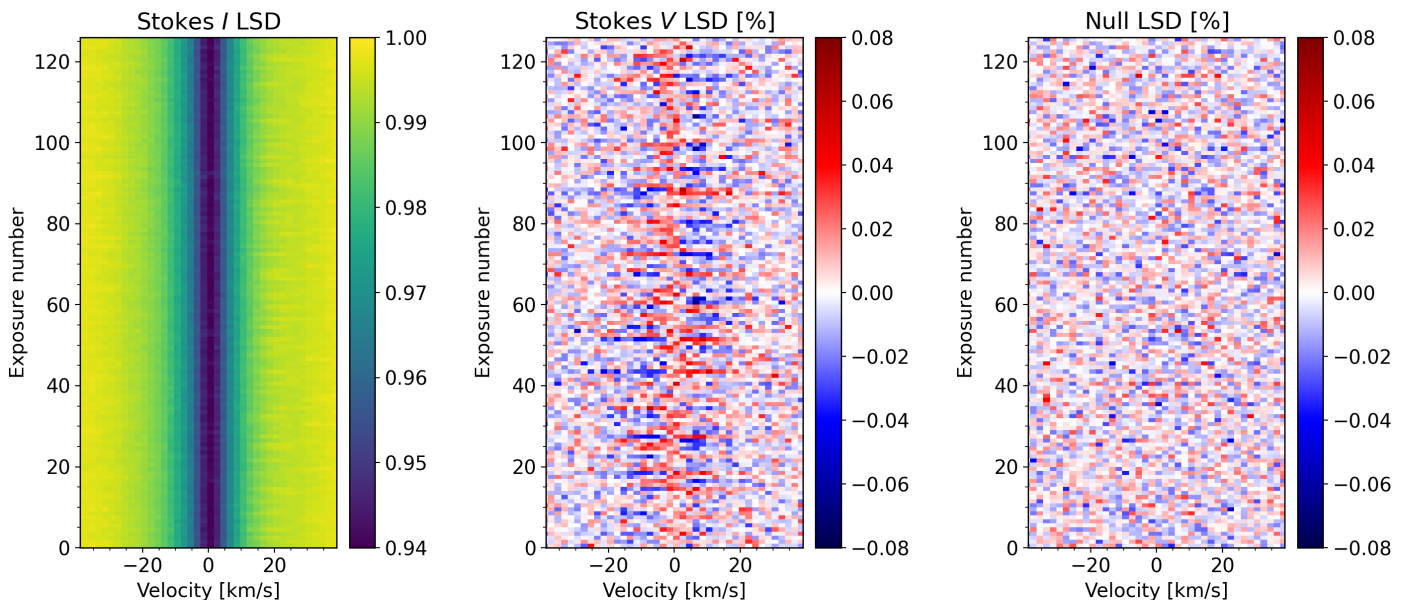


Fig. 1. Dynamical maps of Gl 410 constructed from individual observations (horizontal bands), stacked vertically. The first plot shows Stokes I LSD profiles, where the continuum is given in yellow and the different absorption depths are shown in green and blue shades. The following plots show the Stokes V and null LSD profiles, where positive values are given as red shades, and negative values are shown as blue shades. Note that Stokes V and null LSD amplitudes are expressed in percent. All plots are given in the rest frame of Gl 410 and display a velocity window of 10 FWHM (see Table 1).

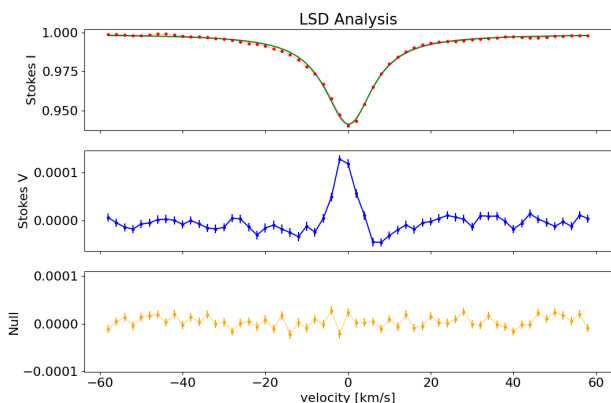


Fig. 2. Median of all LSD profiles in the Gl 410 SPIRou time series. The top panel shows Stokes I LSD (red points) with a Voigt profile model fit (green line), the middle panel shows Stokes V (blue points), and the bottom panel shows the null polarization profile (orange points).

of SPIRou following the same prescription as in Rees & Semel (1979); Donati et al. (1997); Moutou et al. (2020); Martioli et al. (2020). B_ℓ is defined as the brightness-weighted line-of-sight-projected component of the vector magnetic field integrated over the visible hemisphere of the star, and is given in G by

$$B_\ell = -2.142 \times 10^{11} \frac{\int v V(v) dv}{\lambda_0 \cdot g_{\text{eff}} \cdot c \cdot \int [1 - I(v)] dv}, \quad (1)$$

where c is the speed of light in the same unit as v (km s^{-1}), $I(v)$ is the Stokes I LSD profile normalized by the continuum, and $V(v)$ is the Stokes V LSD profile, both as functions of the velocity v in the stellar frame, λ_0 is the mean wavelength in nm, and g_{eff} is the mean Landé factor of the lines included in the LSD analysis.

As the spatial distribution of the magnetic regions may be nonaxisymmetric, B_ℓ can be modulated by the stellar rotation. This allows deriving the stellar rotation period if any periodicity is detected in its time series (e.g., Preston 1971; Landstreet 1980). Examples focusing more on K and M dwarfs can be found in (e.g., Morin et al. 2008; Moutou et al. 2017; Petit et al. 2021). Fig. 5 and Fig. 6 show the generalized Lomb-Scargle (GLS) periodogram (Zechmeister & Kürster 2009) for the B_ℓ data calculated using the tool `astropy.timeseries`¹² for our two example stars Gl 410 and Gl 905. We find a maximum power at a period of 13.9 d for Gl 410 and at 108.6 d for Gl 905, both with a false-alarm probability (FAP) below 0.001%. In the case of Gl 905, three other peaks below an FAP of 0.001% can be noted in the periodogram, and they are due to harmonics of the main period.

As the magnetic field of M dwarfs is likely to evolve with time, this study requires a flexible model to account for the variability. We employed a Gaussian process (GP) regression analysis (e.g., Haywood et al. 2014; Aigrain et al. 2015) using the code `george`¹³ (Ambikasaran et al. 2015), where we assumed that the rotationally modulated stellar activity signal in B_ℓ is quasi-periodic (QP). Thus, we adopted a parameterized covariance function (or kernel) as in Angus et al. (2018), which is given by

$$k(\tau_{ij}) = \alpha^2 \exp \left[-\frac{\tau_{ij}^2}{2l^2} - \frac{1}{\beta^2} \sin^2 \left(\frac{\pi \tau_{ij}}{P_{\text{rot}}} \right) \right] + \sigma^2 \delta_{ij}, \quad (2)$$

where $\tau_{ij} = t_i - t_j$ is the time difference between data points i and j , α^2 is the amplitude of the covariance, l is the decay time, β is the smoothing factor, P_{rot} is the star rotation period, and σ is an additional uncorrelated white noise, which adds a jitter

¹² <https://docs.astropy.org/en/stable/timeseries/lombscargle.html>

¹³ <http://dfm.io/george/current/>

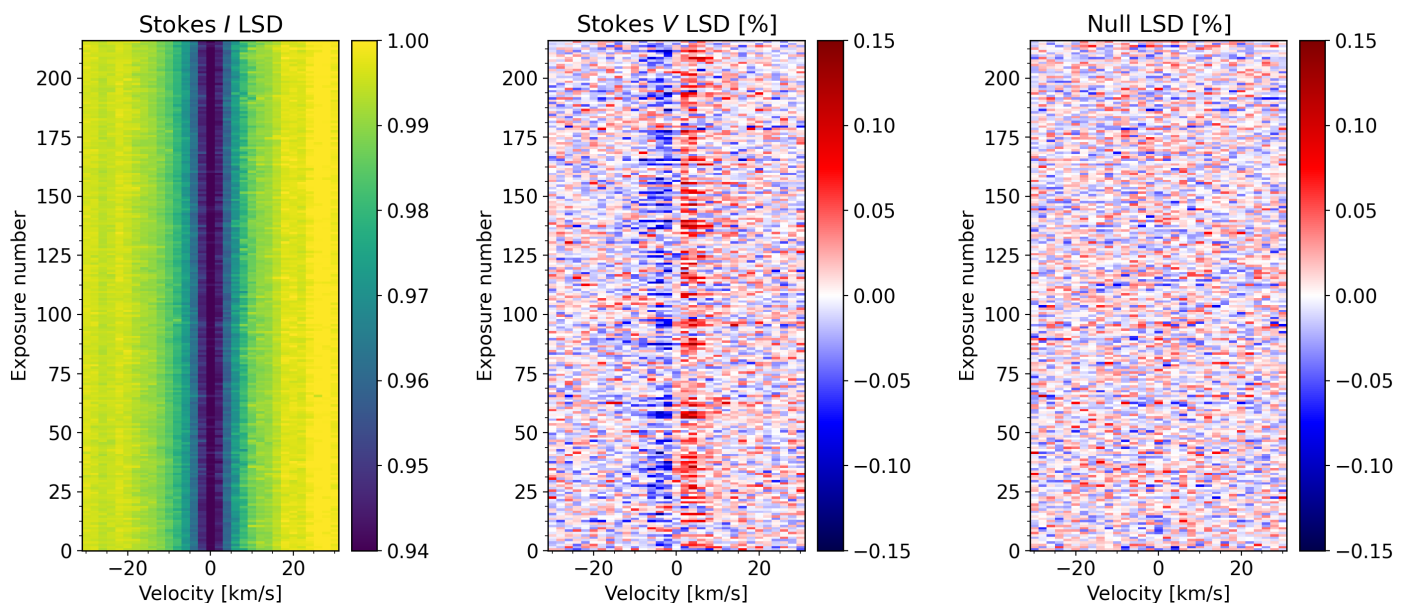


Fig. 3. Similar to Fig. 1, but for the dynamical maps of Stokes I , V and null LSD profiles collected for Gl 905 using SPIRou.

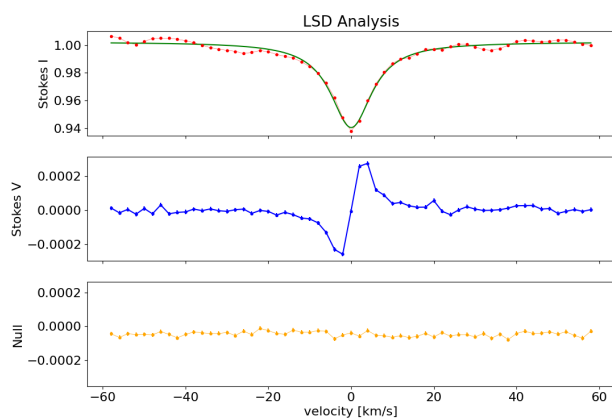


Fig. 4. Median of all LSD profiles in the Gl 905 SPIRou time series. The top panel shows Stokes I LSD (red points) with a Voigt profile model fit (green line), the middle panel shows Stokes V (blue points), and the bottom panel shows the null polarization profile (orange points).

term to the diagonal of the covariance matrix. This kernel combines a squared exponential component describing the overall covariance decay and a component that describes the periodic covariance structure, the amplitude of which is controlled by the smoothing factor¹⁴. Typical values of β vary between 0.25 and 1.25. The lower values correspond to multiple harmonics, and the higher values emphasize single sinusoidal variation. Similarly, the decay parameter varies between a few tens to a few hundred days. As pointed out by Angus et al. (2018), the flexibility of this model can easily lead to an overfitting of the data. To avoid this, we adopted a uniform prior distribution of the parameters (see, e.g., Table 3) that restricts the search range to realistic values. In addition, when the posterior distribution of the smoothing factor and decay time did not display a clear peak, we

¹⁴ The definition of the decay timescale and smoothing factor vary among researchers. The former is sometimes defined as $\sqrt{2}l$ (e.g., Petit et al. 2021), and $1/\beta^2$ may appear as Γ and be called harmonic complexity (e.g., Nicholson & Aigrain 2022).

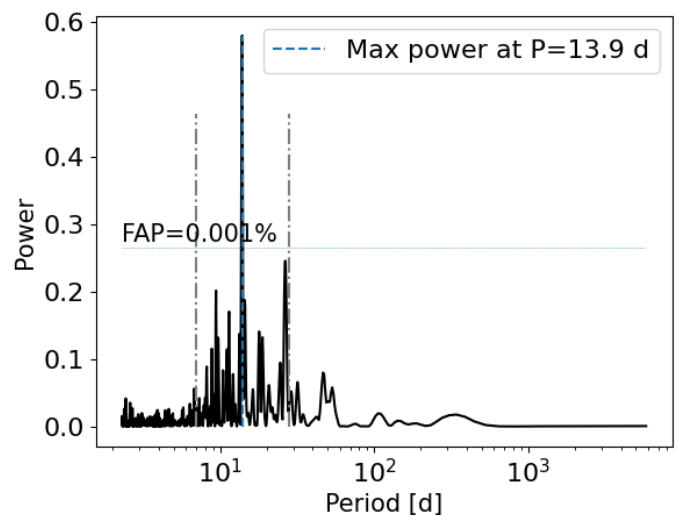


Fig. 5. Generalized Lomb-Scargle periodogram analysis of the longitudinal magnetic field (B_l) time series of Gl 410. The dashed blue line shows the highest power at a period of 13.9 d, and the dot-dashed lines indicate possible harmonics at half and twice the period.

restricted the fit from six to five parameters by fixing the value of the smoothing factor at 0.7, which corresponds to the middle of the range of explored values and to the median value of stars with a constrained smoothing factor. We also explored a four-parameter fit in which both the smoothing factor and the decay time were fixed at 0.7 and 200 days, respectively. We found no significant differences with respect to the five-parameter fit. The value of the fixed decay time is a guess at best and may depend on the spectral type (early-M stars seem to have a shorter decay time, about 70 days): Giles et al. (2017) reported based on Kepler light curves that cooler stars have spots that last much longer, in particular for stars with longer rotational periods.

We used this GP framework to model the B_l data, where we first fit the GP model parameters by maximizing the likelihood function defined in (Eq. 5.8)¹⁵ of Rasmussen & Williams (2006)

¹⁵ <http://gaussianprocess.org/gpml/chapters/RW5.pdf>

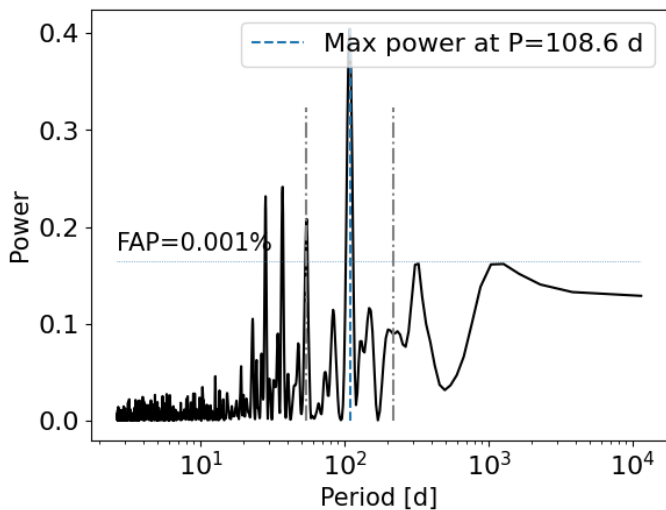


Fig. 6. GLS periodogram analysis of the longitudinal magnetic field (B_ℓ) time series of Gl 905. The dashed blue line shows the highest power at a period of 108.6 d, and the dot-dashed lines indicate possible harmonics at half and twice the period.

and as implemented in *george*, and then we sampled the posterior distribution of the free parameters using a Bayesian Markov chain Monte Carlo (MCMC) framework with the package *mcee* (Foreman-Mackey et al. 2013). We set the MCMC with 50 walkers, 1000 burn-in samples, and 5000 samples. The results of our analysis are illustrated in Fig. 7 and Fig. 9, where we present the observed B_ℓ data and the best-fit GP model for Gl 410 and Gl 905, respectively. Fig. 8 and Fig. 10 show the MCMC samples and posterior distributions of the GP parameters for a six-parameter fit of the B_ℓ time series for Gl 410 and Gl 905, respectively.

4. Results

4.1. Early-type M dwarfs

Our sample includes seven early-M dwarfs (M0V to M2V) with absolute magnitudes in the *Gaia* EDR3 G band between 8 and 9. With masses between $0.5\text{--}0.6 M_\odot$, they are partially convective. To compute the LSD profiles of these stars, we used a mask with atomic lines of the known Landé factor at 4000 K and $\log g=5.0$. For six of them, the longitudinal magnetic field clearly varies, and accordingly, the rotation period is measured quite accurately. We used the six-parameter fit of the quasi-periodic GP model for them, but the decay time could not be well constrained for two of them. They are reported in Table 3, which lists the best-fit parameters measured as the median of the distribution, with uncertainties given by the 0.16 and 0.84 quantiles. Here and in Tables 5 and 8, the number of visits corresponds to the final number after poor polarimetric sequences were rejected, and it therefore differs from the numbers listed in Table 1. Results for Gl 205 were already published in Cortes-Zuleta et al. (2023) based on a similar data set, but with the *Libre-Esprit* data reduction and analysis package: the agreement of the measured parameters is encouraging (see Table 2). The rotation periods lie between 11 and 38 d for this sample. As the radius of early-type M dwarfs is in the range $0.5\text{--}0.6 R_\odot$, these rotation periods translate into equatorial velocities below 3 km s^{-1} . This $v \sin i$ is below the detectability threshold of our spectrograph ($2\text{--}3 \text{ km s}^{-1}$). A broadening in the FWHM of the Stokes I profile may be due to

several factors when the rotation is negligible: for active stars, it may come from a Zeeman broadening effect, but for the quiet stars studied in this sample, it is probably due to other factors. In Sec. 5 we return to this topic after the full sample is analyzed. For the earliest spectral-type star Gl 338B, the Stokes V signal is clearly detected (see Fig. C.1). However, we failed to detect any periodicity in the longitudinal magnetic field variation, probably due to the low number of visits (58 observations).

The GP parameters appear to show that the decay time is pretty well constrained, with values clustering around 75 d. The smoothing parameter varies more widely, between 0.5 (several harmonics) and 1.0 (smooth variation). For two stars with poorly constrained smoothing parameter and decay time, we used a five-parameter fit by fixing the smoothing parameter to 0.7. The white noise is always compatible with 0 within 2σ , meaning that the GP does not need an additional variable to explain the dispersion, and the reduced χ^2 are close to 1. We reach an rms of the fit of a few G for these stars. The results are summarized in Table 3.

Rotation periods were already known for all these stars, based on a variety of indicators: ZDI analysis, photometry (noted "phm" in Tables 4, 6, and 9), and activity indicators (noted "act" in the same tables). In Table 4 we compare our new values to those from the literature. The agreement is good in general, but some literature values are discrepant for unclear reasons (see, e.g., Gl 846) or reveal a harmonic (twice the frequency of rotation: Gl 382 for Sabotta et al. (2021)). Photometry and activity measurements may be affected by sporadic variability (flares), and poor sampling may lead to differences or detection of harmonics of the true rotation period. A case-by-case discussion is difficult as the literature values are based on different techniques with varying precision, time sampling, and total time coverage. For our method, the time sampling and total coverage are generally adequate, and the precision is quite uniform after rejecting low S/N measurements.

4.2. Mid-type M dwarfs

The most numerous subcategory in our sample comprises 26 stars with M_G between 9 and 11, spectral types ranging from M1V to M4V, and masses between 0.2 and $0.5 M_\odot$. This group crosses the so-called Jao gap (Jao et al. 2018) at about $M_G=10.2$, $G_{BP}\text{--}G_{RP}=2.3$, and includes the transition between partially convective and fully convective M dwarfs. As the transition mass between these two regimes is poorly defined (0.2 to $0.35 M_\odot$) and depends on metallicity (see Feiden et al. 2021 for a more detailed discussion), we preferred not to try to define a finer grid of magnitudes or spectral types with the risk of a possibly inhomogeneous subcategory. To compute the LSD profiles of these stars, we used a mask with atomic lines of the known Landé factor at 3500 K and $\log g=5.0$.

In contrast with the group of early-M dwarfs, here only half of the stars have a detected rotation period. We first tried a six-parameter fit of the quasi-periodic GP model for them, but only three stars have a well-constrained decay time at about 100 days. For the other stars for which we were able to determine a rotation period, we use a five or even a four parameters fit, fixing the smoothing parameter at 0.7 (five-parameter fit), and when necessary, the decay time to 200 days (four-parameter fit). We detect a very long periodic variation of about 450 days for Gl 411 in this group, which clearly disagrees with the shorter period reported from photometry by Díaz et al. (2019) of 56.15 ± 0.27 d, and is unexpectedly long compared to all the M dwarfs with known stellar rotation periods (see Fig. 11). It would imply an unknown mechanism of angular momentum loss. We show the GP fit in

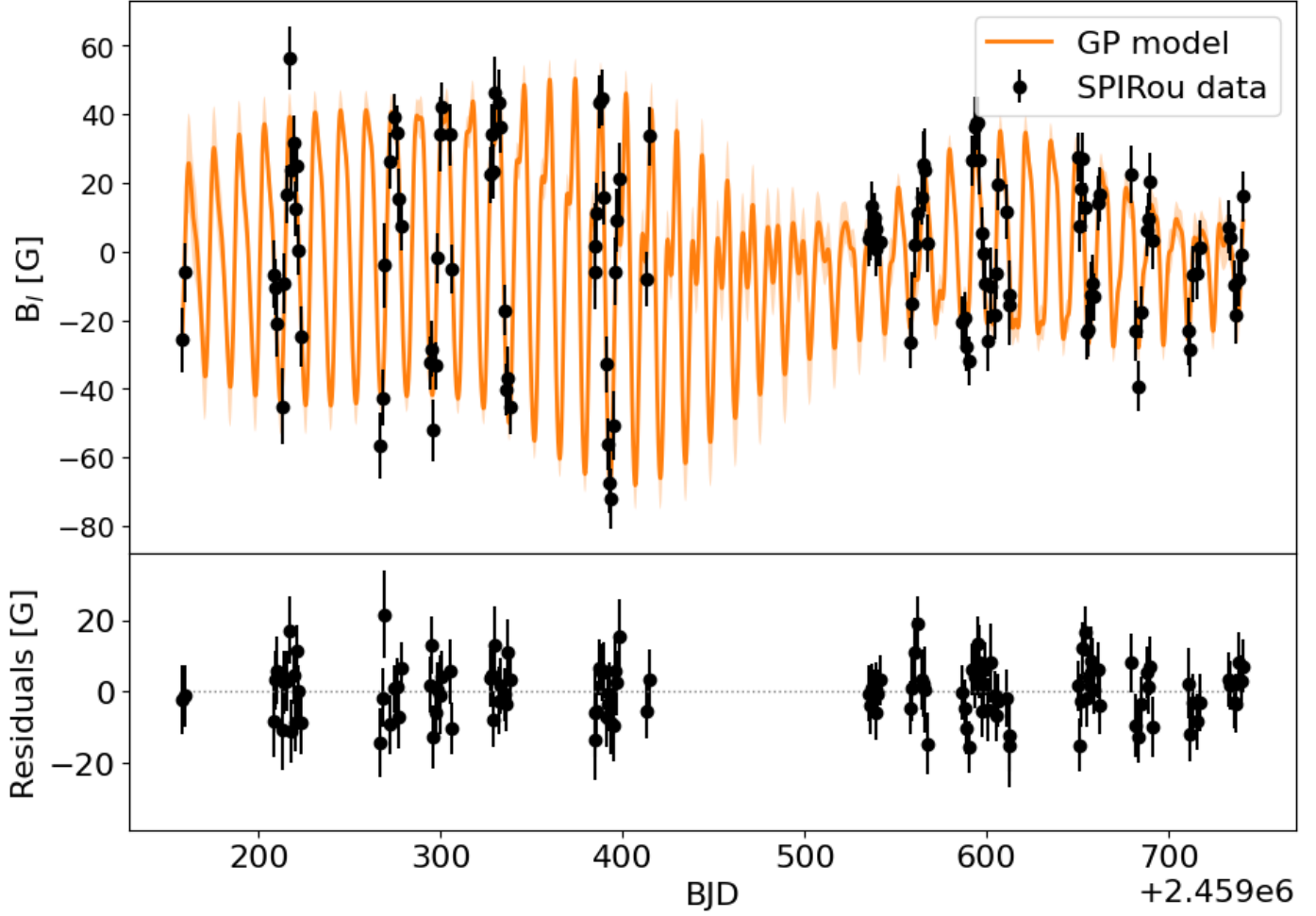


Fig. 7. GP analysis of the SPIRou B_ℓ data of Gl 410. In the top panel, the black points show the observed B_ℓ data, and the orange line shows the best-fit quasi-periodic GP model. The bottom panel shows the residuals with an RMS dispersion of 7.6 G.

Table 2. Best six-parameter fit of a quasi-periodic GP model obtained in our analysis of the stellar activity from the SPIRou B_ℓ data of Gl 205, compared to the results from Cortes-Zúñiga et al. (2023) using a similar data set, but the *Libre-Esprit* data reduction and analysis package.

Package	rotation period P_{rot} [d]	mean B_ℓ μ [G]	white noise σ [G]	amplitude α [G]	decay time l [d]	smoothing factor β	rms [G]	χ_{red}^2	visits
APER0	$34.3^{+0.4}_{-0.4}$	$2.5^{+2.0}_{-2.0}$	$1.0^{+0.5}_{-0.6}$	$7.1^{+1.3}_{-1.0}$	67^{+15}_{-11}	$0.54^{+0.09}_{-0.07}$	2.5	0.79	152
Libre-Esprit	$34.4^{+0.5}_{-0.4}$	$1.3^{+0.9}_{-0.9}$	$0.4^{+0.2}_{-0.2}$	$3.1^{+0.6}_{-0.4}$	63^{+13}_{-8}	$0.57^{+0.10}_{-0.08}$	0.94	0.84	153

Table 3. Best six-parameter fit of a quasi-periodic GP model obtained in our analysis of the stellar activity from the SPIRou B_ℓ data of the early-type M dwarfs in our sample.

Star	rotation period P_{rot} [d]	mean B_ℓ μ [G]	white noise σ [G]	amplitude α [G]	decay time l [d]	smoothing factor β	rms [G]	χ_{red}^2	visits
Priors	$\mathcal{U}(2, 300)$	$\mathcal{U}(-\infty, +\infty)$	$\mathcal{U}(0, +\infty)$	$\mathcal{U}(0, +\infty)$	$\mathcal{U}(50, 1000)$	$\mathcal{U}(0.25, 1.25)$			
Gl 846	$11.01^{+0.17}_{-0.22}$	$-0.6^{+2.0}_{-2.1}$	$2.6^{+1.0}_{-1.3}$	$6.2^{+1.4}_{-1.2}$	57^{+18}_{-5}	$0.96^{+0.19}_{-0.22}$	6.1	1.05	188
Gl 205	$34.3^{+0.4}_{-0.4}$	$2.5^{+2.0}_{-2.0}$	$1.0^{+0.5}_{-0.6}$	$7.1^{+1.3}_{-1.0}$	67^{+15}_{-11}	$0.54^{+0.09}_{-0.07}$	2.5	0.79	152
Gl 410	$13.87^{+0.08}_{-0.07}$	$-1.1^{+10.8}_{-10.5}$	$3.7^{+2.0}_{-2.2}$	$28.9^{+6.7}_{-4.7}$	78^{+16}_{-14}	$0.73^{+0.13}_{-0.10}$	7.6	0.86	126
Gl 880	$37.7^{+0.8}_{-0.6}$	$4.0^{+3.4}_{-3.1}$	$0.8^{+0.8}_{-0.6}$	$11.4^{+2.4}_{-1.7}$	94^{+24}_{-20}	$0.56^{+0.10}_{-0.08}$	3.8	0.65	162
Gl 514	$30.45^{+0.13}_{-0.14}$	$-4.2^{+5.9}_{-5.4}$	$2.1^{+1.3}_{-1.4}$	$8.8^{+3.6}_{-2.4}$		$0.99^{+0.18}_{-0.25}$	8.2	1.10	165
Gl 382	$21.32^{+0.04}_{-0.03}$	$-0.7^{+4.2}_{-4.2}$	$2.8^{+1.2}_{-1.5}$	$7.9^{+3.2}_{-1.9}$		$0.62^{+0.27}_{-0.18}$	6.7	1.11	114

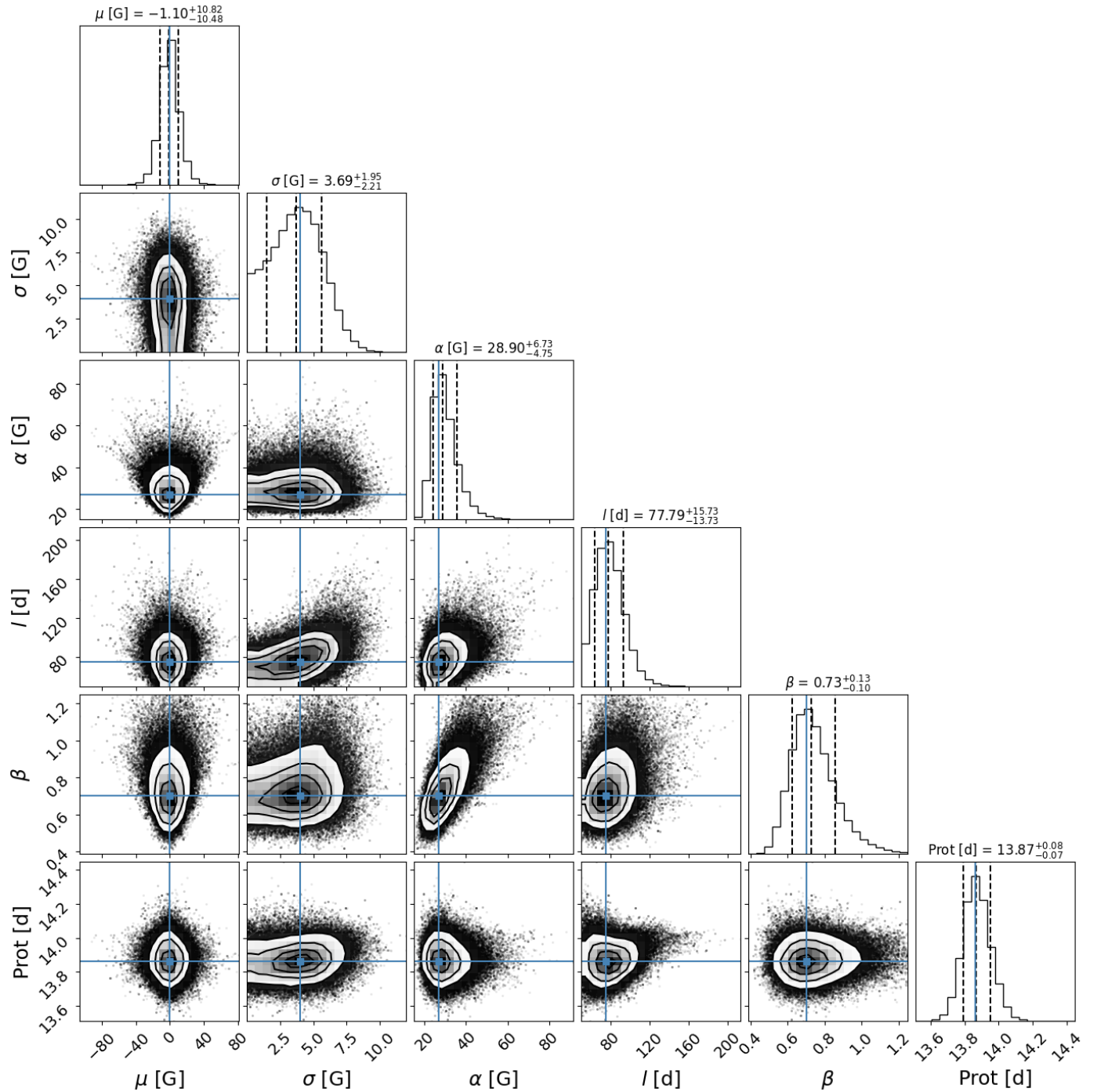


Fig. 8. MCMC samples and the posterior distributions of parameters in the quasi-periodic GP analysis of the stellar activity in the SPIRou B_l data of Gl 410. The blue crosses mark the mode of the distribution, and the vertical dashed lines in the histograms indicate the median and the 16 and 84 percentiles of the posterior PDF. The shaded regions correspond to uncertainties of 1, 2, and 3 σ in order of increasing radius.

Fig. B.1 that corresponds to this particular star, and its associated corner plot is presented in Fig. B.3. The measured period may correspond to a cyclic variation in the magnetic field that is more related to the variation of the activity than to the stellar rotation.

We were able to measure the rotation period for half of the mid-M dwarfs compared to 100% for the early-M dwarfs. Furthermore, a six-parameter fit could only be measured for three stars compared to four out of six for the early-M dwarfs. This may come from a longer decay time that is not constrained enough by our three-year survey. The shape of the variation in

the longitudinal magnetic field varies strongly, from almost sinusoidal variations for Gl 169.1A (smoothing factor of 1) to a variation featuring only a few harmonics for Gl 48, GJ 3378 or GJ 4333 (smoothing factor of 0.6). The amplitude of the variations ranges from very weak (5 G for Gl 411) to about 20 G for GJ 4333 and Gl 876. For this group, the white-noise component of the GP is always compatible with 0 at 2σ , as was the case for the early-M dwarfs.

In Table 6 we compare our new values of the rotation period to those from the literature. The agreement is good in general, but some literature values are discrepant. Excluding pos-

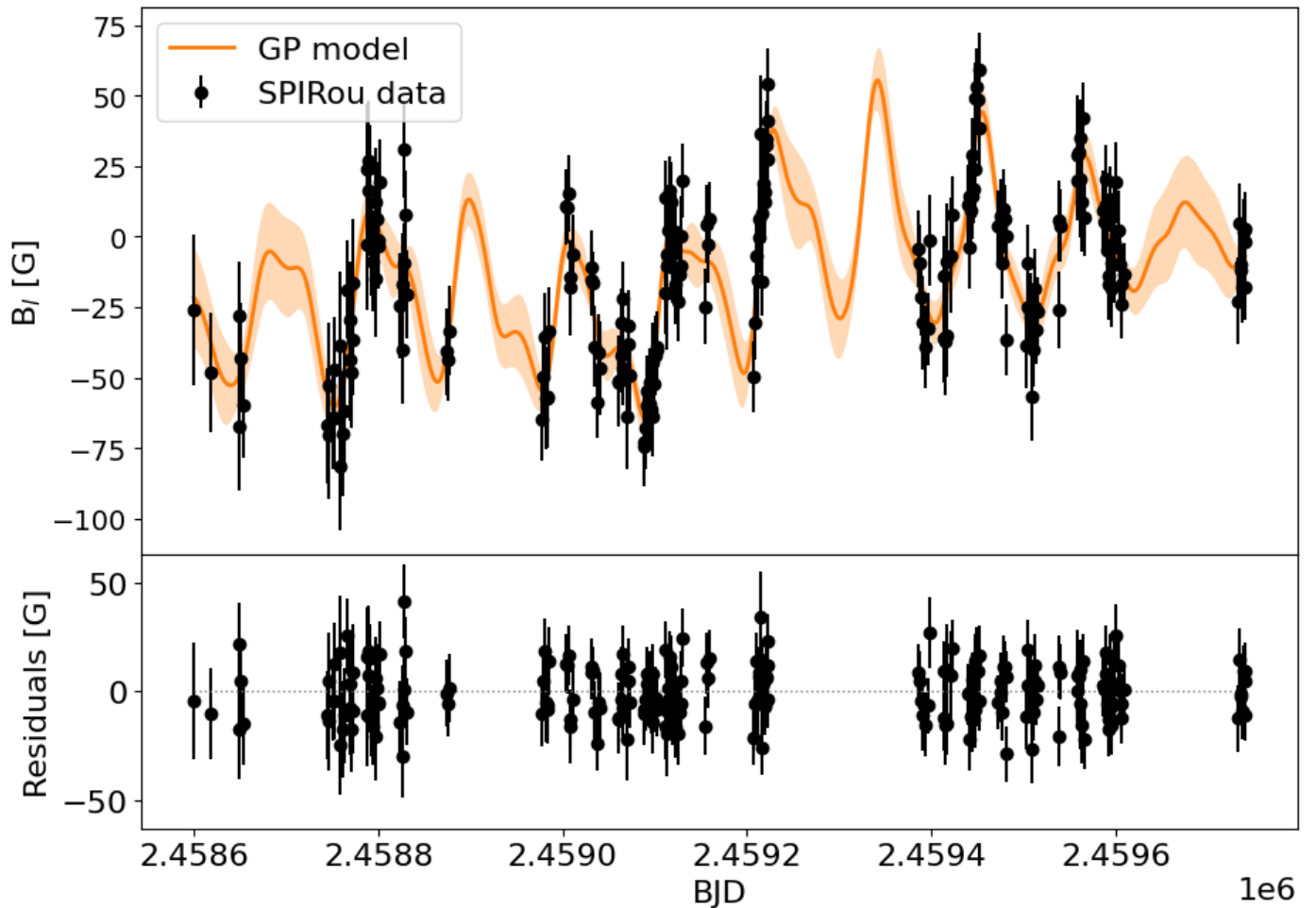


Fig. 9. GP analysis of the SPIRou B_ℓ data of G1905. In the top panel, the black points show the observed B_ℓ data, and the orange line shows the six-parameter best-fit quasi-periodic GP model. The bottom panel shows the residuals with an RMS dispersion of 13 G.

Table 4. Comparison of the rotation periods given in the literature with our measured values for the early-M stars.

Reference	Category	G1205	G1382	G1410	G1514	G1846	G1880
This work	B_ℓ	34.3 ± 0.4	21.32 ± 0.04	13.87 ± 0.08	30.45 ± 0.14	11.01 ± 0.20	37.7 ± 0.7
Kiraga & Stepien (2007)	phm	33.61	21.56				
Donati et al. (2008)	ZDI			14.0			
Bonfils et al. (2013)	act	32.8, 39.3				10.7	
Suárez Mascareño et al. (2015)	act	35.0 ± 0.1	21.7 ± 0.1		28.0 ± 2.9	31.0 ± 0.1	37.5 ± 0.1
Suárez Mascareño et al. (2016)	phm	33.4 ± 0.1	21.2 ± 0.1				
Hébrard et al. (2016)	ZDI	33.63 ± 0.37		13.83 ± 0.10		10.73 ± 0.10	
Suárez Mascareño et al. (2017)	act	34.8 ± 1.3	21.8 ± 0.1		30.0 ± 0.9	26.3 ± 5.6	37.2 ± 6.7
Díez Alonso et al. (2019)	phm	33.8 ± 0.6	21.6 ± 0.2	14.6 ± 0.2		29.5 ± 0.1	39.5 ± 0.2
Sabotta et al. (2021)	act	37.08	10.65, 21.4				

sible sampling problems or a low number of measurements in one case (G1876), there may be more fundamental reasons for some techniques to succeed or fail on a given star: photometric variations may be affected by flares, while the longitudinal magnetic field of the star may stay constant due to an axisymmetric field topology that prevents us from detecting a periodic variation even when the Stokes V profiles show a clear detection. At least in one case, G1411, the very long measured period may in fact reflect a cyclic variation of activity rather than the stellar rotation period. We also show at the end of Sec. 4.3 that some stars

have a clear detection of the Stokes V profile, but no rotation period detected when the magnetic field is axisymmetric.

We also tested the results of the Libre-Esprit pipeline as given in Carmona et al. (in prep) for G1388 (AD Leo), even though this star was discarded from our sample because it is too active. Table 7 compares the results, which agree excellently well.

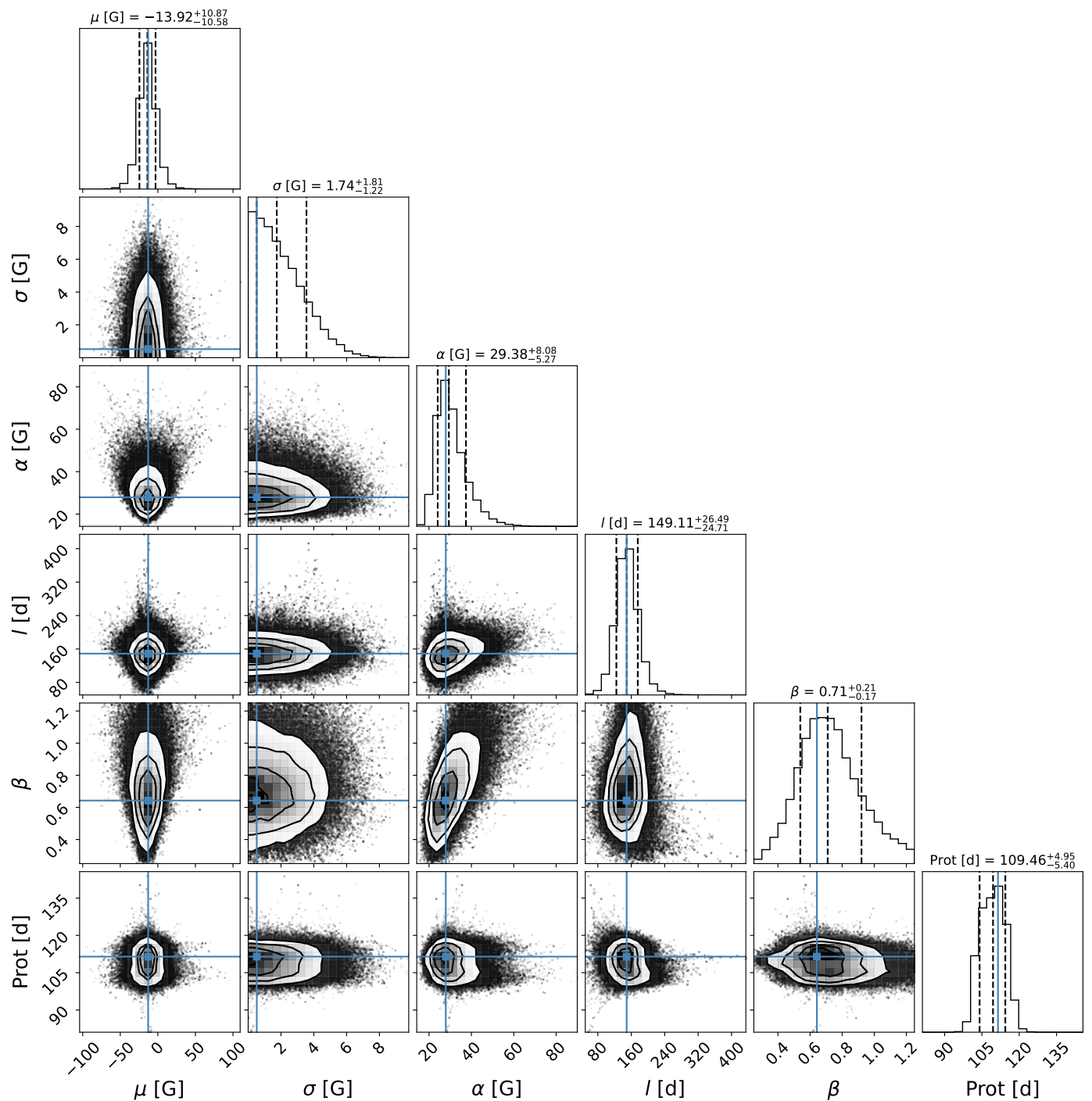


Fig. 10. MCMC samples and the posterior distributions of the six-parameter fit of a quasi-periodic GP on the SPIRou B_ℓ data of G1905. The same format is used as in Fig. 8.

4.3. Late-M dwarfs

The last group contains ten stars with M_G above 11 (up to 13.5), spectral types from M3.5V to M5.5V, and masses between 0.1 and 0.2 M_\odot . These stars are fully convective. Stars with later spectral types (M6.0V and M6.5V) in the WP1 sample are all active stars with short rotation periods and are therefore excluded from this study. To compute the LSD profiles of these late-type stars, we used a mask with atomic lines of the known Landé factor at 3000 K and $\log g=5.0$. We generally had to use a four-parameter fit of the quasi-periodic GP model for them, fixing the smoothing parameter to 0.7 and the decay time to 200 days,

except for two stars in this group, for which a six-parameter fit gives well-constrained values of the smoothing factor and the decay time. The others are marked with an asterisk in Table 8. For only one star, G1447 (Ross 128, FI Vir), are we unable to confirm the long rotation period measured from ASAS photometry by Suárez Mascareño et al. (2016) (165.1 ± 0.8 d) and Díez Alonso et al. (2019) (163 ± 3 d). This is probably due to the low number and distribution of the visits (57, clustered into two groups) compared to the other late-M dwarfs, which prevents us from determining the rotation period of G1447. This highlights once again that our set limit to 50 visits with adequate sampling

Table 5. Best six to four parameters fit of a quasi-periodic GP model obtained in our analysis of the stellar activity from the SPIRou B_ℓ data of the mid-range M dwarfs in our sample. The asterisk after a star name means that the measured period is more uncertain and was obtained by a five or four parameters fit only.

Star	rotation period P_{rot} [d]	mean B_ℓ μ [G]	white noise σ [G]	amplitude α [G]	decay time l [d]	smoothing factor β	rms [G]	χ^2_{red}	visits
Priors	$\mathcal{U}(2, 300)$	$\mathcal{U}(-\infty, +\infty)$	$\mathcal{U}(0, +\infty)$	$\mathcal{U}(0, +\infty)$	$\mathcal{U}(50, 1000)$	$\mathcal{U}(0.25, 1.25)$			
Gl 752A	53.2 ^{+5.5} _{-3.0}	0.2 ^{+3.4} _{-3.2}	1.6 ^{+1.3} _{-1.1}	8.6 ^{+2.9} _{-1.9}	93 ⁺⁵⁵ ₋₂₉	0.89 ^{+0.24} _{-0.29}	6.2	0.87	128
Gl 48	51.2 ^{+1.4} _{-1.4}	-7.0 ^{+3.6} _{-3.7}	1.8 ^{+1.6} _{-1.2}	10.2 ^{+3.2} _{-2.1}	112 ⁺⁵⁵ ₋₃₆	0.62 ^{+0.22} _{-0.16}	9.4	0.86	188
Gl 15A	44.3 ^{+2.0} _{-2.0}	-1.0 ^{+1.8} _{-1.7}	1.0 ^{+0.9} _{-0.7}	5.4 ^{+1.4} _{-1.0}	85 ⁺³⁶ ₋₂₂	0.71 ^{+0.28} _{-0.23}	5.6	0.82	246
Gl 849	41.4 ^{+0.4} _{-0.4}	4.7 ^{+6.3} _{-5.9}	2.4 ^{+1.6} _{-1.6}	12.1 ^{+5.1} _{-3.2}		0.87 ^{+0.24} _{-0.23}	10.0	1.01	185
Gl 411	471 ⁺⁴¹ ₋₄₀	5.9 ^{+2.4} _{-2.1}	0.8 ^{+0.8} _{-0.6}	4.2 ^{+1.8} _{-1.1}		0.68 ^{+0.32} _{-0.27}	6.3	0.94	212
Gl 687	56.5 ^{+1.3} _{-0.5}	4.9 ^{+8.9} _{-6.4}	1.7 ^{+1.3} _{-1.1}	13.3 ^{+7.3} _{-4.3}		0.97 ^{+0.19} _{-0.26}	8.2	1.10	214
Gl 725A	103.5 ^{+4.6} _{-5.1}	-14.9 ^{+3.4} _{-3.1}	1.2 ^{+1.2} _{-0.8}	8.7 ^{+2.4} _{-1.6}			8.1	0.81	214
Gl 251*	98.7 ^{+11.5} _{-4.8}	17.4 ^{+3.6} _{-3.6}	1.7 ^{+1.6} _{-1.2}	8.3 ^{+2.4} _{-1.9}			9.9	0.85	177
GJ 4333*	72.0 ^{+0.9} _{-1.2}	6.8 ^{+8.9} _{-8.0}	2.6 ^{+2.1} _{-1.7}	18.5 ^{+8.9} _{-4.1}		0.55 ^{+0.25} _{-0.17}	12.7	0.83	190
Gl 876	82.8 ^{+2.0} _{-0.7}	3.5 ^{+13.3} _{-13.5}	2.0 ^{+1.9} _{-1.4}	23.0 ^{+12.3} _{-7.1}		0.72 ^{+0.24} _{-0.19}	8.5	0.92	88
PM J09553-2715*	70.5 ^{+5.7} _{-1.9}	15.4 ^{+9.8} _{-11.7}	2.7 ^{+2.4} _{-1.9}	15.1 ^{+8.7} _{-5.1}		0.82 ^{+0.30} _{-0.33}	11.8	0.91	74
GJ 3378*	92.1 ^{+4.1} _{-5.3}	13.6 ^{+5.6} _{-5.4}	4.6 ^{+2.3} _{-2.7}	12.0 ^{+5.1} _{-2.8}		0.61 ^{+0.32} _{-0.23}	13.9	1.00	174
Gl 169.1A	91.9 ^{+4.1} _{-2.6}	2.3 ^{+8.4} _{-7.2}	1.9 ^{+1.9} _{-1.3}	11.4 ^{+5.3} _{-3.3}		1.04 ^{+0.15} _{-0.23}	13.4	0.91	172

Table 6. Comparison of the rotation periods given in the literature with our measured values for the mid-M stars.

Reference	Category	Gl 752A	Gl 48	Gl 15A	Gl 849	Gl 411	Gl 687	Gl 251	GJ 4333	Gl 876	Gl 3378
This work	B_ℓ	53 ± 4	51.2 ± 1.4	44.3 ± 2.0	41.4 ± 0.4	470 ± 40	56.5 ± 0.9	99 ± 8	72.0 ± 1.0	82.8 ± 1.4	92 ± 5
Rivera et al. (2005)	phm									96.7 ± 1.0	
Bonfils et al. (2013)	act				2000 ?					61.0, 30.1	
Burt et al. (2014)	phm						61.8 ± 1.0				
Howard et al. (2014)	phm			43.82 ± 0.56							
Suárez Mascareño et al. (2015)	act	46.5 ± 0.3			39.2 ± 6.3					87.3 ± 5.7	
Nelson et al. (2016)	act									95 ± 1	
Suárez Mascareño et al. (2016)	phm	46.0 ± 0.2									
Moutou et al. (2017)	ZDI							90 ± 10			
Suárez Mascareño et al. (2017)	act									90.9 ± 16.5	
Suárez Mascareño et al. (2018)	act			45.0 ± 4.4							
Díaz et al. (2019)	phm					56.15 ± 0.27					
Díaz Alonso et al. (2019)	phm	46.0 ± 0.2	51.5 ± 2.6					18.1 ± 0.3	74.7 ± 0.7	81.0 ± 0.8	
Reinhold & Hekker (2020)	phm									31.31 ± 8.15	
Stock et al. (2020)	phm							122.1 ± 2.2			
Sabotta et al. (2021)	act	174.48	43.39					67.59, 119.48			83.39

Table 7. Best six-parameter fit of a quasi-periodic GP model obtained in our analysis of the stellar activity from the SPIRou B_ℓ data of Gl 388 (AD Leo), compared to the results from Carmona et al. (in prep) using a similar data set, but the Libre-Esprit data reduction and analysis package.

Package	rotation period P_{rot} [d]	mean B_ℓ μ [G]	white noise σ [G]	amplitude α [G]	decay time l [d]	smoothing factor β	rms [G]	χ^2_{red}	visits
APER0	2.2301 ^{+0.0019} _{-0.0017}	-156 ⁺⁴³ ₋₄₂	4.6 ^{+3.3} _{-3.0}	68 ⁺²¹ ₋₁₄	220 ⁺⁴¹ ₋₄₀	1.35 ^{+0.11} _{-0.19}	12.7	0.91	70
Libre-Esprit	2.2304 ^{+0.0015} _{-0.0013}	-156 ⁺⁴⁷ ₋₄₄	5.4 ^{+3.7} _{-3.6}	67 ⁺²³ ₋₁₅	255 ⁺⁹⁶ ₋₇₇	1.36 ^{+0.10} _{-0.17}	14.7	0.96	69

is essential. Below this value, the determination of the rotation period becomes difficult.

In Table 9 we compare our new rotation periods to those from the literature. The agreement is not as good as for earlier M dwarfs, probably because their rotation periods are longer and the uncertainties are larger. It becomes naturally harder to determine very long periods as we are limited by the time range of the SPIRou observations.

Finally, in Table 10, we present the data of the 16 stars for which we were unable to measure a rotation period. For these stars, we arbitrarily fixed the decay parameter to 200 d and the smoothing factor to 0.7 to obtain some indications about the mean B_ℓ , residual white noise, and amplitude of the field. The GP also gives a value of the rotation period, but we do not list it as it is not well constrained. We assumed that the values of the other parameters of the GP still bear some information, although the fact that the rotation period is not constrained and that two

Table 8. Best six, five, or four parameters fit of a quasi-periodic GP model obtained in our analysis of the stellar activity from the SPIRou B_ℓ data of the late-M dwarfs in our sample. The asterisk after a star name means that the measured period is more uncertain and was obtained by a four-parameter fit only.

Star	rotation period P_{rot} [d]	mean B_ℓ μ [G]	white noise σ [G]	amplitude α [G]	decay time l [d]	smoothing factor β	rms [G]	χ_{red}^2	visits
Priors	$\mathcal{U}(2, 300)$	$\mathcal{U}(-\infty, +\infty)$	$\mathcal{U}(0, +\infty)$	$\mathcal{U}(0, +\infty)$	$\mathcal{U}(50, 1000)$	$\mathcal{U}(0.25, 1.25)$			
GJ 1289	$74.0^{+1.5}_{-1.3}$	47^{+25}_{-25}	$2.4^{+2.5}_{-1.7}$	67^{+21}_{-12}	142^{+33}_{-26}	$0.64^{+0.17}_{-0.11}$	14.7	0.67	180
GJ 1103*	139^{+22}_{-23}	$8.2^{+10.1}_{-10.1}$	$4.1^{+4.0}_{-2.9}$	$18.2^{+8.9}_{-5.9}$			16.4	0.83	62
Gl 699*	$137.1^{+6.8}_{-4.0}$	$3.0^{+5.7}_{-5.8}$	$1.1^{+1.1}_{-0.8}$	$14.7^{+3.0}_{-2.4}$			8.7	0.77	243
Gl 15B*	$116.5^{+6.4}_{-4.7}$	$-0.3^{+6.3}_{-6.2}$	$2.1^{+2.1}_{-1.4}$	$13.8^{+3.8}_{-2.8}$			16.5	0.78	184
GJ 1151*	158^{+14}_{-9}	$-9.6^{+13.4}_{-13.2}$	$2.7^{+2.6}_{-1.9}$	$29.6^{+8.2}_{-5.5}$			15.7	0.83	153
Gl 905	$109.5^{+4.9}_{-5.4}$	-14^{+11}_{-11}	$1.7^{+1.8}_{-1.2}$	$29.4^{+8.1}_{-5.3}$	149^{+26}_{-25}	$0.71^{+0.21}_{-0.17}$	12.6	0.73	216
GJ 1286*	203^{+14}_{-21}	36^{+19}_{-20}	$5.7^{+4.5}_{-3.8}$	44^{+14}_{-10}			25.0	0.89	108
GJ 1002	$93.0^{+1.4}_{-1.7}$	$-6.4^{+12.5}_{-14.2}$	$4.1^{+3.4}_{-2.8}$	$20.4^{+9.7}_{-5.9}$		$0.90^{+0.24}_{-0.31}$	19.9	1.05	154

Table 9. Comparison of the rotation periods given in the literature with our measured values for the late Ms.

Reference	Category	GJ 1289	Gl 699	GJ 1151	Gl 905	GJ 1286	GJ 1002
This work	B_ℓ	74.0 ± 1.4	137 ± 5	158 ± 12	110 ± 5	203 ± 18	93.0 ± 1.6
Benedict et al. (1998)	phm		130.4				
Irwin et al. (2011)	phm			132			
Suárez Mascareño et al. (2015)	act		148.6 ± 0.1				
Moutou et al. (2017)	ZDI	54 ± 4					
Newton et al. (2018)	phm					88.92	
Toledo-Adrón et al. (2019)	phm		145 ± 15				
Díez Alonso et al. (2019)	phm	83.6 ± 7.0		125 ± 23	106 ± 6		
Sabotta et al. (2021)	act		311.25		178.74		
Suárez Mascareño et al. (2022)	act						126 ± 15

parameters of the GP are arbitrarily fixed limits the value of this information. For completeness, we list a period and its reference, when available in the literature, but this information was not used in our GP fit.

The Stokes V profiles in Appendix C may tentatively explain these nondetections by their magnetic topology: if the magnetic field is axisymmetric, we cannot detect the rotation modulation. To test this interpretation, we measured the rate of detection of Stokes V profiles for a given star by comparison to the noise measured in a velocity region well outside of the line. We find that this metric quantifies the visual impression of the time series of Stokes V profiles quite well, as shown in Appendix C. Then, we subtracted a median Stokes V profile for each star and measured the detection rate again. For some stars, it changes dramatically, and we tentatively interpret this change by the subtraction of a constant component due to an axisymmetric magnetic field. This is the case of Gl 408, Gl 338B, Gl 436, GJ 4063, and Gl 617B. For other stars, the detection rate does not significantly change when the median-subtracted profiles are compared to the original Stokes V profiles. This is the case of PMJ21463+3813, Gl 412A, PMJ08402+3127, Gl 480, and GJ 1148 among the stars without a detected rotation period. We plan a more detailed study of the magnetic topology of the stars

in our sample to further investigate the reasons for these nondetections.

5. Discussion and conclusions

We have shown that spectropolarimetry is a useful technique for measuring the rotation period of a star, even for quiet M dwarfs. In our sample of 43 such stars, we were able to reliably measure the rotation period for 27 stars, 8 of which were previously unknown. The rotation periods cover a wide range in this sample of quiet stars, from 10 to 450 days. The agreement with other techniques, such as photometry or stellar activity indicators is good, except for a few stars (e.g., Gl 251, Gl 411, and Gl 846) for which some techniques find a harmonic of the rotation period or converge toward very different values. The amplitude of variation in the longitudinal magnetic field for these quiet M dwarfs ranges from 3 G (Gl 338B, Gl 445) to 20 G for the majority of the stars in our sample, but it can reach up to 70 G in some cases (GJ 1289), which is comparable to more active stars such as AD Leo (Gl 388: 45 ± 6 G, Carmona et al., in prep) or EV Lac (Gl 873: 149 ± 17 G) over the same period of observations. The FWHM of the median Stokes I profile is another important measurement, as it may reveal a broadening due to the Zeeman effect for active stars. As the FWHM is sensitive to

Table 10. Best four-parameter fit of a quasi-periodic GP model obtained in our analysis of the stellar activity from the SPIRou B_ℓ data of the M dwarfs in our sample without a clear periodic variation detection.

Star	mean B_ℓ μ [G]	white noise σ [G]	amplitude α [G]	rms [G]	χ^2_{red}	number of visits	rotation period from literature P_{rot} [d]	reference
Priors	$\mathcal{U}(-\infty, +\infty)$	$\mathcal{U}(0, +\infty)$	$\mathcal{U}(0, +\infty)$					
Gl 338B	$-8.1^{+1.6}_{-1.6}$	$1.3^{+1.0}_{-0.9}$	$3.1^{+1.6}_{-1.4}$	4.4	1.03	58	16.66	Sabotta et al. (2021)
Gl 617B	$19.3^{+4.0}_{-4.0}$	$1.4^{+1.5}_{-1.0}$	$8.9^{+2.9}_{-2.1}$	8.2	0.71	142		
Gl 412A	$13.7^{+4.1}_{-4.3}$	$4.0^{+1.2}_{-1.4}$	$10.7^{+3.5}_{-2.5}$	9.7	1.23	174	100.9 ± 0.3	Suárez Mascareño et al. (2018)
Gl 480	$6.6^{+3.5}_{-3.3}$	$5.5^{+1.8}_{-2.1}$	$6.9^{+2.8}_{-2.3}$	11.0	1.28	104		
Gl 436	$-10.4^{+2.2}_{-2.0}$	$1.6^{+1.6}_{-1.1}$	$4.4^{+2.1}_{-1.7}$	7.5	0.81	85	44.09 ± 0.08	Bourrier et al. (2018)
Gl 408	$-43.8^{+3.6}_{-3.6}$	$1.4^{+1.4}_{-1.0}$	$8.7^{+2.6}_{-2.0}$	9.1	0.79	168		
Gl 317	$-10.8^{+8.4}_{-8.8}$	$2.7^{+2.5}_{-1.9}$	$14.5^{+8.2}_{-4.1}$	11.9	0.97	76		
GJ 4063	$17.8^{+3.3}_{-3.2}$	$2.9^{+1.9}_{-1.9}$	$7.1^{+2.3}_{-1.8}$	11.4	0.96	204	40.2 ± 0.8	Díez Alonso et al. (2019)
GJ 1012	$6.4^{+2.6}_{-2.6}$	$3.2^{+2.7}_{-2.2}$	$4.0^{+3.8}_{-2.7}$	15.9	0.99	135		
GJ 1148	$-9.1^{+3.9}_{-3.5}$	$2.3^{+2.4}_{-1.6}$	$7.1^{+4.1}_{-2.9}$	13.9	0.81	101	71.5 ± 5.1	Díez Alonso et al. (2019)
PM J08402+3127	16^{+20}_{-21}	$4.6^{+3.8}_{-3.1}$	39^{+16}_{-9}	18.8	0.98	139	118 ± 14	Díez Alonso et al. (2019)
Gl 725B	$-4.6^{+5.2}_{-5.1}$	$1.2^{+1.3}_{-0.8}$	$12.1^{+3.7}_{-2.8}$	10.7	0.75	209		
GJ 1105	$1.2^{+3.6}_{-3.1}$	$2.4^{+2.2}_{-1.7}$	$7.3^{+3.2}_{-2.7}$	13.5	0.93	161		
Gl 445	$-1.8^{+2.7}_{-2.6}$	$3.4^{+3.2}_{-2.4}$	$3.2^{+3.7}_{-2.3}$	17.4	0.97	90		
PM J21463+3813	$-0.4^{+7.5}_{-7.7}$	$3.1^{+3.1}_{-2.2}$	$16.3^{+6.6}_{-4.6}$	20.7	0.84	176		
Gl 447	$20.5^{+9.1}_{-9.5}$	$4.8^{+3.0}_{-3.0}$	$16.6^{+8.5}_{-5.3}$	14.9	1.13	57	165.1 ± 0.8	Suárez Mascareño et al. (2016)

the total magnetic field (small and large scale), while the longitudinal magnetic field is more sensitive to the large-scale field, a large amplitude of variation in the longitudinal field does not necessarily correlate with a high FWHM, and both measures are therefore important. The average value over our sample is 6.07 km s^{-1} , with a standard deviation of 0.66 km s^{-1} . This is clearly larger than the mean uncertainty of each FWHM in Table 1. This shows a real dispersion among the mean FWHM values, which will be further investigated by using different line lists (low and high Landé factors) and by studying the time variation in the measured FWHM for a given star, as in Bellotti et al. (in prep) for AD Leo.

We divided our sample into three sub-categories according to the absolute magnitude in *Gaia* G band, roughly corresponding to early-, mid- and late-M dwarfs. There is a clear tendency to lower values of the FWHM of the median Stokes I profile toward mid-type stars, with averages and standard deviations for the three groups of 6.65 and 0.59 km s^{-1} (early type), 5.73 and 0.34 km s^{-1} (mid type), and 6.49 and 0.75 km s^{-1} (late type), respectively. The larger dispersion in the early-type and late-type groups may be due to a few active outliers: removing Gl 410 from the early-type group gives new average and standard deviation of 6.45 and 0.40 km s^{-1} , respectively, while for the late-type group, removing GJ 1286 and GJ 1289 gives 6.14 and 0.52 km s^{-1} , respectively, now more compatible with the mid-type group, given the small size of the early- and late-type groups. The most extreme values correspond to Gl 411 ($4.93 \pm 0.18 \text{ km s}^{-1}$) and Gl 410 ($7.73 \pm 0.21 \text{ km s}^{-1}$). A test on GJ 1289 shows that the measured FWHM clearly depends on the minimum adopted depth (0.03 in this work) and the LSD mask (3000 and 3500 K give different results for this 3238 K star), and does not clearly show an increase when using masks limited to low Landé factors ($g_{\text{eff}} \leq 1.2$) versus high Landé factors ($g_{\text{eff}} > 1.2$). The possible effect of the magnetic field on the Stokes I FWHM of the stars in this sample will be studied in detail in Donati et al. (in prep) and Cristofari et al. (in prep).

We observe that it is easier to constrain the rotation period and the other parameters of the GP for early-type stars, even if the amplitude of variation of the longitudinal magnetic field is similar in the other two subcategories. This may be due to the fact that they are brighter than later M dwarfs on average. Additionally, the decay time seems well constrained between 50 and 100 days for the early-type stars. For the mid-M dwarfs, it lies around 100 days, and for the late-M dwarfs, it seems to be longer at about 150 days, although these results are only based on three and two measurements, respectively. There is a tendency for longer decay times for a longer stellar rotation period. Clearly, the quasi-periodic GP fit converges more easily for the early-type stars than for the others: it converges for only 60% of the mid-type stars, and although the convergence rate is similar for the late- and early-type stars, we have to use a four-parameter fit for the late-type stars (fixing the smoothing factor and the decay time), while we can use a six-parameter fit for the early-type stars with good constraints on the smoothing factor and on the decay time.

Our sample is too small to infer general properties of M stars. Therefore, we compare in Fig. 11 the sample of stars analyzed in this paper to more complete nonmagnetic studies in which active and inactive stars are well represented. We include a total of 212 M stars from Newton et al. (2017), whose mass and rotation periods are similar to the range explored in this paper. Our sample of quiet stars nicely fits the sequence of inactive stars, as expected. The long rotation period of Gl 411 appears as an exception, and may in fact not reflect the stellar rotation period, as discussed in Sec. 4.2.

Low-mass stars arrive rapidly rotating on the main sequence and spin down with time as angular momentum is lost through magnetized winds (Barnes 2007). Empirically calibrated relations between age and period can be used to estimate the ages of individual field stars. Gaidos et al. (2023) combined the 4 Gyr M-dwarf gyrochrone of the open cluster M 67 (Dunee et al. 2022) with those of younger, previously published gyrochrones

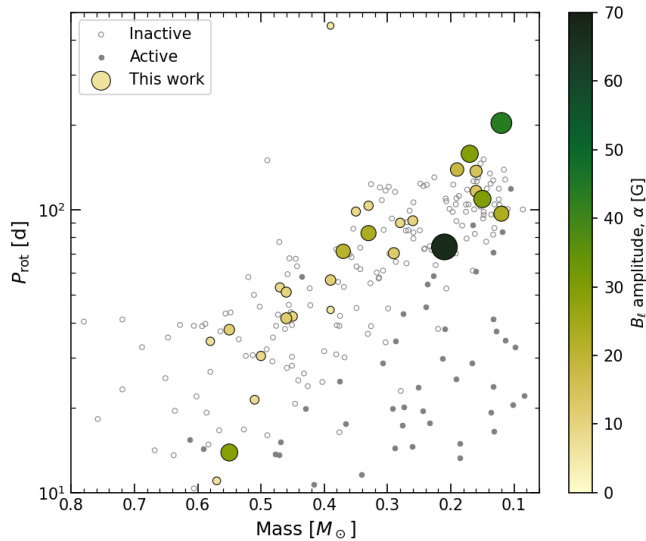


Fig. 11. Rotation period vs stellar mass diagram. Stars with rotation periods determined in this work are shown as larger circles, where the symbol sizes and colors are proportional to the amplitude of variation of B_l (see α values given in Tables 3, 5, and 8). Rotation periods and mass determinations for inactive (white circles) and active (gray circles) stars from Newton et al. (2017) are shown for comparison.

(Curtis et al. 2020) to assign ages to M dwarf host stars with $T_{\text{eff}} = 3200\text{--}4200$ K. We used the same gyrochronology to estimate the ages of 20 stars in our sample with well-measured rotation periods and T_{eff} in that range. Mean values and standard deviations were calculated from distributions constructed by 10000 Monte Carlo calculations, incorporating uncertainties from P_{rot} (from Tables 5 and 8), the gyrochrones, T_{eff} (assumed ± 75 K), $[\text{Fe}/\text{H}]$ (assumed to be ± 0.1 dex), and variation in the initial rotation periods of the stars on the zero-age main sequence. The results are listed in Table 11: most stars are 4–10 Gyr old, and a few younger stars have ages from 0.5 to 2 Gyr. The rotation-age relations are only valid for stars of approximately solar metallicity, but we list in the table (col. 6) a correction computed using a theory-based model and the stellar metallicity, to be added to the age given in col. 4. We report the age for members of binaries, but we emphasize that these stars may have distinct rotational histories due to tides and rapid dissipation of primordial disks (Fleming et al. 2019; Messina 2019).

Our study only exploited the longitudinal magnetic field measured from the spectropolarimetric data of the SPIRou SLS. The same data can be used to achieve much more, for example, to investigate the magnetic topology of these stars and its evolution using ZDI maps.

Acknowledgements. Based on observations obtained at the Canada-France-Hawaii Telescope (CFHT) which is operated from the summit of Maunakea by the National Research Council of Canada, the Institut National des Sciences de l’Univers of the Centre National de la Recherche Scientifique of France, and the University of Hawaii. The observations at the Canada-France-Hawaii Telescope were performed with care and respect from the summit of Maunakea which is a significant cultural and historic site.

This work has made use of data from the European Space Agency (ESA) mission *Gaia* (<https://www.cosmos.esa.int/gaia>), processed by the *Gaia* Data Processing and Analysis Consortium (DPAC, <https://www.cosmos.esa.int/web/gaia/dpac/consortium>). Funding for the DPAC has been provided by national institutions, in particular, the institutions participating in the *Gaia* Multilateral Agreement.

This research has also made intensive use of the SIMBAD database and of the Vizier catalog access tool, operated at CDS, Strasbourg, France and of NASA’s Astrophysics Data System (ADS).

We made an extensive use of the DACE (Data Analysis Center for Exoplanets) software from the University of Geneva (Díaz et al. 2014; Delisle et al. 2016). This work has made use of the VALD database, operated at Uppsala University, the Institute of Astronomy RAS in Moscow, and the University of Vienna.

X.D., A.C., P.C.Z., E.M. and S.B. and more generally most of the French authors of this paper acknowledge funding from the French National Research Agency (ANR) under contract number ANR18CE310019 (SPLaSH). This work is supported by the ANR in the framework of the *Investissements d’Avenir* program (ANR-15-IDEX-02), through the funding of the “Origin of Life” project of the Grenoble-Alpes University.

E.M. acknowledges funding from the *Fundação de Amparo à Pesquisa do Estado de Minas Gerais* (FAPEMIG) under the project number APQ-02493-22.

B.Z. acknowledges funding from the *Programa de Internacionalização da Coordenação de Aperfeiçoamento de Pessoal de Nível Superior* (CAPES-PrInt #88887.683070/2022-00) and FAPEMIG (APQ-01033-22).

J.-F.D. acknowledges funding from the European Research Council (ERC) under the H2020 research & innovation programme (grant agreement #740651 New-Worlds).

N.J.C., E.A. and R.D. wish to thank the Natural Sciences and Engineering Research Council of Canada and the *Fonds Québécois de Recherche - Nature et Technologies*, the *Observatoire du Mont-Mégantic* and the Institute for Research on Exoplanets and acknowledge funding from *Développement Économique Canada*, *Quebec’s Ministère de l’Éducation et de l’Innovation*, the Trotter Family Foundation and the Canadian Space Agency.

This research made use of the hosting service github and, among others, of the following software tools: matplotlib (Hunter 2007); NumPy (Harris et al. 2020); SciPy (Virtanen et al. 2020); Astropy (Astropy Collaboration et al. 2013, 2018); emcee (Foreman-Mackey et al. 2013); corner (Foreman-Mackey 2016); george (Ambikasaran et al. 2015); barrycorpy (Wright & Eastman 2014).

References

- Aigrain, S., Hodgkin, S. T., Irwin, M. J., Lewis, J. R., & Roberts, S. J. 2015, *MNRAS*, 447, 2880
- Ambikasaran, S., Foreman-Mackey, D., Greengard, L., Hogg, D. W., & O’Neil, M. 2015, *IEEE Transactions on Pattern Analysis and Machine Intelligence*, 38, 252
- Angus, R., Morton, T., Aigrain, S., Foreman-Mackey, D., & Rajpaul, V. 2018, *MNRAS*, 474, 2094
- Artigau, É., Astudillo-Defru, N., Delfosse, X., et al. 2014, in *Society of Photo-Optical Instrumentation Engineers (SPIE) Conference Series*, Vol. 9149, Proc. SPIE, 914905
- Artigau, É., Cadieux, C., Cook, N. J., et al. 2022, *AJ*, 164, 84
- Astropy Collaboration, Price-Whelan, A. M., Sipőcz, B. M., et al. 2018, *AJ*, 156, 123
- Astropy Collaboration, Robitaille, T. P., Tollerud, E. J., et al. 2013, *A&A*, 558, A33
- Babcock, H. W. 1947, *ApJ*, 105, 105
- Bagnulo, S., Landolfi, M., Landstreet, J. D., et al. 2009, *PASP*, 121, 993
- Bakos, G., Noyes, R. W., Kovács, G., et al. 2004, *PASP*, 116, 266
- Barnes, S. A. 2007, *ApJ*, 669, 1167
- Benedict, G. F., McArthur, B., Nelan, E., et al. 1998, *AJ*, 116, 429
- Boisse, I., Bouchy, F., Hébrard, G., et al. 2011, *A&A*, 528, A4
- Bonfils, X., Delfosse, X., Udry, S., et al. 2013, *A&A*, 549, A109
- Bonfils, X., Mayor, M., Delfosse, X., et al. 2007, *A&A*, 474, 293
- Bourrier, V., Lovis, C., Beust, H., et al. 2018, *Nature*, 553, 477
- Burt, J., Vogt, S. S., Butler, R. P., et al. 2014, *ApJ*, 789, 114
- Cook, N. J., Artigau, É., Doyon, R., et al. 2022, *PASP*, 134, 114509
- Cortes-Zuleta, P., Boisse, I., Klein, B., et al. 2023, *arXiv e-prints*, arXiv:2301.10614
- Cristofari, P. I., Donati, J. F., Masseron, T., et al. 2022, *MNRAS*, 516, 3802
- Curtis, J. L., Agüeros, M. A., Matt, S. P., et al. 2020, *ApJ*, 904, 140
- Delisle, J. B., Ségransan, D., Buchschacher, N., & Alesina, F. 2016, *A&A*, 590, A134
- Díaz, R. F., Almenara, J. M., Santerne, A., et al. 2014, *MNRAS*, 441, 983
- Díaz, R. F., Delfosse, X., Hobson, M. J., et al. 2019, *A&A*, 625, A17
- Díez Alonso, E., Caballero, J. A., Montes, D., et al. 2019, *A&A*, 621, A126
- Donati, J. F., Kouach, D., Moutou, C., et al. 2020, *MNRAS*, 498, 5684
- Donati, J. F., Morin, J., Petit, P., et al. 2008, *MNRAS*, 390, 545
- Donati, J. F., Semel, M., Carter, B. D., Rees, D. E., & Collier Cameron, A. 1997, *MNRAS*, 291, 658
- Dungee, R., van Saders, J., Gaidos, E., et al. 2022, *ApJ*, 938, 118
- Faria, J. P., Adibekyan, V., Amazo-Gómez, E. M., et al. 2020, *A&A*, 635, A13
- Feiden, G. A., Skidmore, K., & Jao, W.-C. 2021, *ApJ*, 907, 53
- Figueira, P., Santos, N. C., Bonfils, X., et al. 2010, in *EAS Publications Series*, Vol. 42, *EAS Publications Series*, ed. K. Goździewski, A. Niedzielski, & J. Schneider, 131–135

Table 11. Gyrochronological ages of the stars in our sample. Errors on T_{eff} and $[M/H]$ are assumed to be 75 K and 0.1 dex. The correction in the last column corresponds to the value to be added to the age due to the nonsolar metallicity of the star.

Star	T_{eff} K	P_{rot} d	Age Gyr	$[M/H]$ dex	Metallicity correction Gyr
Gl 846	3833	11.01 ± 0.20	< 0.53	0.07	0.1
Gl 410	3842	13.87 ± 0.08	0.89 ± 0.12	0.05	0.1
Gl 382	3644	21.32 ± 0.04	1.9 ± 0.6	0.15	0.2
Gl 514	3699	30.45 ± 0.14	3.8 ± 0.6	-0.07	-0.1
GJ 1289	3238	74.0 ± 1.4	3.8 ± 1.2	0.05	0.0
Gl 849	3502	41.4 ± 0.4	4.2 ± 1.0	0.35	0.4
Gl 205	3771	34.3 ± 0.4	5.2 ± 0.7	0.43	0.6
PM J09553-2715	3366	70.5 ± 3.8	5.2 ± 2.0	-0.03	-0.0
Gl 880	3702	37.7 ± 0.7	5.5 ± 0.8	0.26	0.4
Gl 169.1A	3307	91.9 ± 3.4	5.5 ± 2.4	0.13	0.1
Gl 687	3475	56.5 ± 0.9	5.9 ± 1.8	0.01	0.0
Gl 15A	3611	44.3 ± 0.2	6.0 ± 1.2	-0.33	-0.5
GJ 3378	3326	92.1 ± 4.7	6.0 ± 2.7	-0.05	-0.0
Gl 48	3529	51.2 ± 1.4	6.1 ± 1.6	0.08	0.1
Gl 15B	3272	116.5 ± 5.6	6.1 ± 3.0	-0.42	-0.2
Gl 876	3366	82.8 ± 1.4	6.2 ± 2.7	0.15	0.1
Gl 752A	3558	53.2 ± 4.2	7.1 ± 1.9	0.11	0.2
Gl 699	3311	137.1 ± 5.4	9.4 ± 5.0	-0.37	-0.2
Gl 251	3420	98.7 ± 8.2	10.8 ± 4.7	-0.01	-0.0
Gl 725A	3470	103.5 ± 4.8	14.8 ± 5.4	-0.26	-0.3

- Fleming, D. P., Barnes, R., Davenport, J. R. A., & Luger, R. 2019, *ApJ*, 881, 88
- Foreman-Mackey, D. 2016, *The Journal of Open Source Software*, 1, 24
- Foreman-Mackey, D., Hogg, D. W., Lang, D., & Goodman, J. 2013, *PASP*, 125, 306
- Gaia Collaboration, Brown, A. G. A., Vallenari, A., et al. 2021, *A&A*, 649, A1
- Gaidos, E., Claytor, Z., Dungee, R., Ali, A., & Feiden, G. A. 2023, *MNRAS*[arXiv:2301.12109]
- Giles, H. A. C., Collier Cameron, A., & Haywood, R. D. 2017, *MNRAS*, 472, 1618
- Gustafsson, B., Edvardsson, B., Eriksson, K., et al. 2008, *A&A*, 486, 951
- Harris, C. R., Millman, K. J., van der Walt, S. J., et al. 2020, *Nature*, 585, 357
- Haywood, R. D., Collier Cameron, A., Queloz, D., et al. 2014, *MNRAS*, 443, 2517
- Hébrard, É. M., Donati, J. F., Delfosse, X., et al. 2016, *MNRAS*, 461, 1465
- Henry, G. W. 1999, *PASP*, 111, 845
- Hobson, M. J., Bouchy, F., Cook, N. J., et al. 2021, *A&A*, 648, A48
- Horne, K. 1986, *PASP*, 98, 609
- Howard, A. W., Marcy, G. W., Fischer, D. A., et al. 2014, *ApJ*, 794, 51
- Huélamo, N., Figueira, P., Bonfils, X., et al. 2008, *A&A*, 489, L9
- Hunter, J. D. 2007, *Computing In Science & Engineering*, 9, 90
- Irwin, J., Berta, Z. K., Burke, C. J., et al. 2011, *ApJ*, 727, 56
- Irwin, J., Charbonneau, D., Nutzman, P., & Falco, E. 2009, in *Transiting Planets*, ed. F. Pont, D. Sasselov, & M. J. Holman, Vol. 253, 37–43
- Jao, W.-C., Henry, T. J., Gies, D. R., & Hambly, N. C. 2018, *ApJ*, 861, L11
- Kane, S. R., Thirumalachari, B., Henry, G. W., et al. 2016, *ApJ*, 820, L5
- Kanodia, S. & Wright, J. 2018, *Research Notes of the AAS*, 2, 4
- Kiraga, M. & Stepien, K. 2007, *Acta Astron.*, 57, 149
- Lafarga, M., Ribas, I., Reiners, A., et al. 2021, *arXiv e-prints*, arXiv:2105.13467
- Landi Degl'Innocenti, E. 1992, in *Solar Observations: Techniques and Interpretation*, ed. F. Sanchez, M. Collados, & M. Vazquez, 71
- Landstreet, J. D. 1980, *AJ*, 85, 611
- Landstreet, J. D. 1992, *A&A Rev.*, 4, 35
- Mann, A. W., Dupuy, T., Kraus, A. L., et al. 2019, *ApJ*, 871, 63
- Martiofi, E., Hébrard, G., Moutou, C., et al. 2020, *A&A*, 641, L1
- Messina, S. 2019, *A&A*, 627, A97
- Morin, J., Donati, J. F., Petit, P., et al. 2008, *MNRAS*, 390, 567
- Morin, J., Donati, J. F., Petit, P., et al. 2010, *MNRAS*, 407, 2269
- Moutou, C., Dalal, S., Donati, J. F., et al. 2020, *A&A*, 642, A72
- Moutou, C., Hébrard, E. M., Morin, J., et al. 2017, *MNRAS*, 472, 4563
- Nelson, B. E., Robertson, P. M., Payne, M. J., et al. 2016, *MNRAS*, 455, 2484
- Newton, E. R., Irwin, J., Charbonneau, D., et al. 2017, *ApJ*, 834, 85
- Newton, E. R., Mondrik, N., Irwin, J., Winters, J. G., & Charbonneau, D. 2018, *AJ*, 156, 217
- Nicholson, B. A. & Aigrain, S. 2022, *MNRAS*, 515, 5251
- Noyes, R. W., Weiss, N. O., & Vaughan, A. H. 1984, *ApJ*, 287, 769
- Nutzman, P. & Charbonneau, D. 2008, *PASP*, 120, 317
- Petit, P., Folsom, C. P., Donati, J. F., et al. 2021, *A&A*, 648, A55
- Piskunov, N. E., Kupka, F., Ryabchikova, T. A., Weiss, W. W., & Jeffery, C. S. 1995, *A&AS*, 112, 525
- Pojmanski, G. 1997, *Acta Astron.*, 47, 467
- Pollacco, D. L., Skillen, I., Collier Cameron, A., et al. 2006, *PASP*, 118, 1407
- Preston, G. W. 1971, *PASP*, 83, 571
- Queloz, D., Henry, G. W., Sivan, J. P., et al. 2001, *A&A*, 379, 279
- Rasmussen, C. E. & Williams, C. K. I. 2006, *Gaussian Processes for Machine Learning* (MIT Press)
- Rees, D. E. & Semel, M. D. 1979, *A&A*, 74, 1
- Reinhold, T. & Hekker, S. 2020, *A&A*, 635, A43
- Rivera, E. J., Lissauer, J. J., Butler, R. P., et al. 2005, *ApJ*, 634, 625
- Robertson, P. & Mahadevan, S. 2014, *ApJ*, 793, L24
- Robertson, P., Mahadevan, S., Endl, M., & Roy, A. 2014, *Science*, 345, 440
- Ryabchikova, T., Piskunov, N., Kurucz, R. L., et al. 2015, *Phys. Scr.*, 90, 054005
- Sabotta, S., Schlecker, M., Chaturvedi, P., et al. 2021, *A&A*, 653, A114
- Stock, S., Nagel, E., Kemmer, J., et al. 2020, *A&A*, 643, A112
- Suárez Mascareño, A., González-Álvarez, E., Zapatero Osorio, M. R., et al. 2022, *arXiv e-prints*, arXiv:2212.07332
- Suárez Mascareño, A., Rebolo, R., & González Hernández, J. I. 2016, *A&A*, 595, A12
- Suárez Mascareño, A., Rebolo, R., González Hernández, J. I., & Esposito, M. 2015, *MNRAS*, 452, 2745
- Suárez Mascareño, A., Rebolo, R., González Hernández, J. I., & Esposito, M. 2017, *MNRAS*, 468, 4772
- Suárez Mascareño, A., Rebolo, R., González Hernández, J. I., et al. 2018, *A&A*, 612, A89
- Toledo-Padrón, B., González Hernández, J. I., Rodríguez-López, C., et al. 2019, *MNRAS*, 488, 5145
- Virtanen, P., Gommers, R., Oliphant, T. E., et al. 2020, *Nature Methods*, 17, 261
- West, A. A., Hawley, S. L., Bochanski, J. J., et al. 2008, *AJ*, 135, 785
- Woźniak, P. R., Vestrand, W. T., Akerlof, C. W., et al. 2004, *AJ*, 127, 2436
- Wright, J. T. & Eastman, J. D. 2014, *PASP*, 126, 838
- Zechmeister, M. & Kürster, M. 2009, *A&A*, 496, 577

Appendix A: Quasi-periodic Gaussian process regression for stars with a measured rotation period

We display here the temporal evolution of the longitudinal magnetic field and its GP fit leading to the measurement of the stellar rotation period for 25 stars of our sample (Figs. A.1 to A.24). GP fits are generally six-parameter fits, except when stated in the caption.

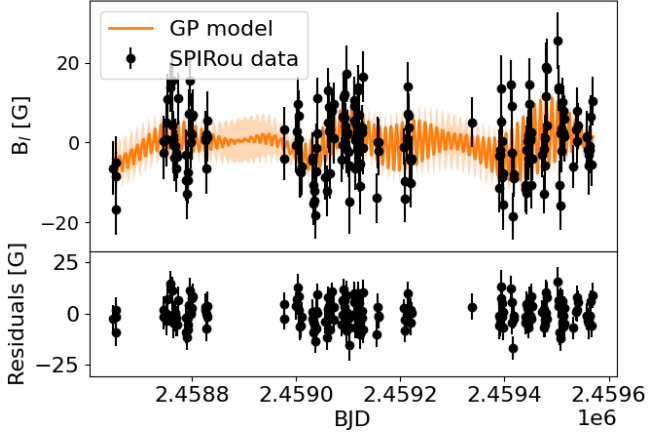


Fig. A.1. GP analysis of the SPIRou B_ℓ data of Gl 846. The top panel shows the observed B_ℓ data (black points) and the orange line shows the best-fit quasi-periodic GP model. The bottom panel shows the residuals.

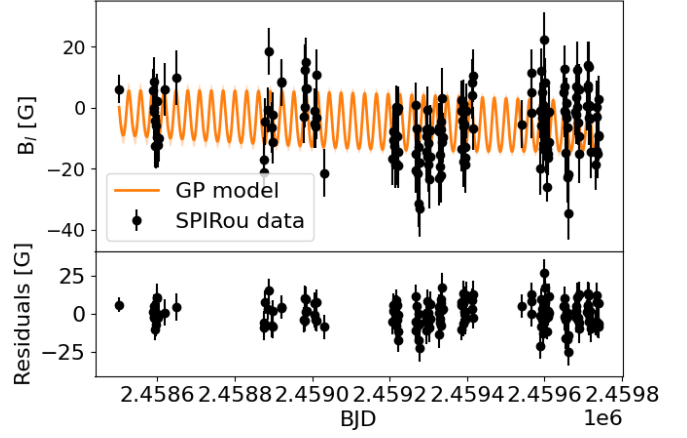


Fig. A.4. Same for Gl 514.

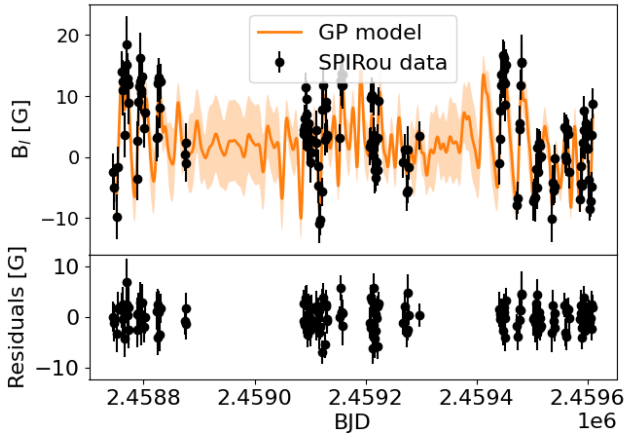


Fig. A.2. Same for Gl 205.

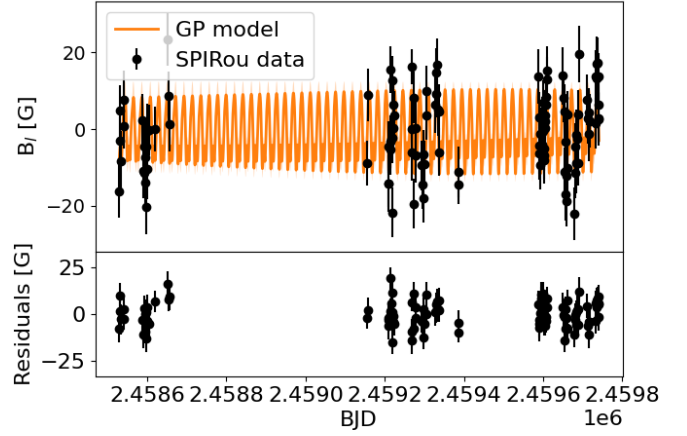


Fig. A.5. Same for Gl 382.

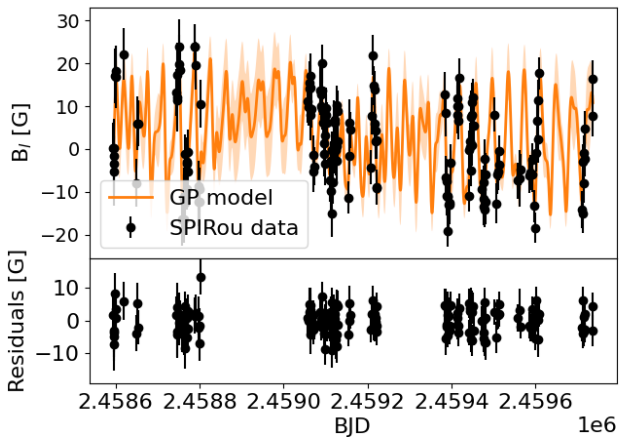


Fig. A.3. Same for Gl 880.

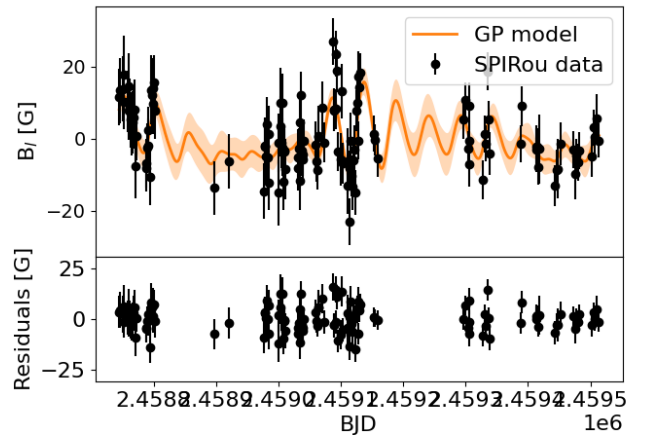


Fig. A.6. Same for Gl 752A.

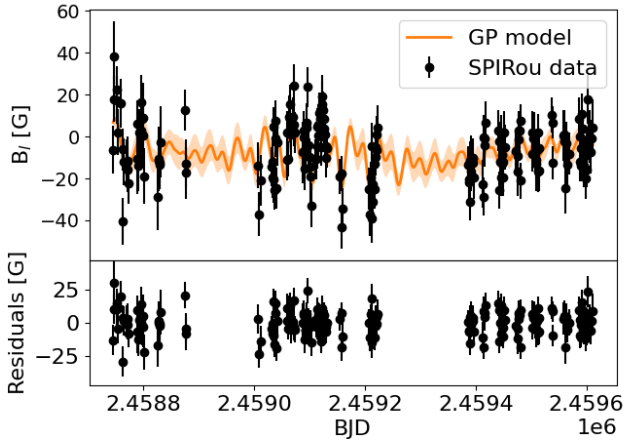


Fig. A.7. Same for GI 48.

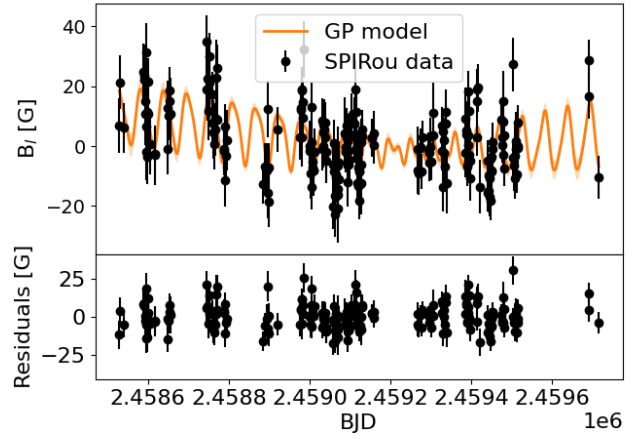


Fig. A.10. Same for GI 687.

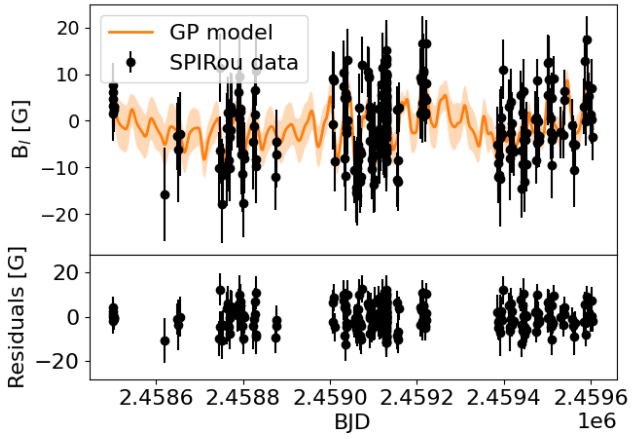


Fig. A.8. Same for GI 15A.

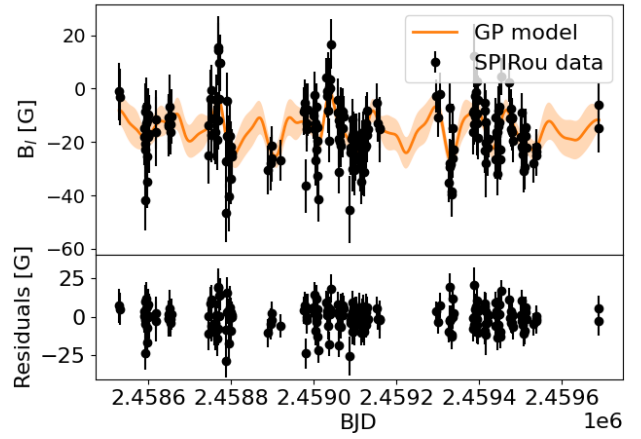


Fig. A.11. Same for GI 725A (five-parameter fit).

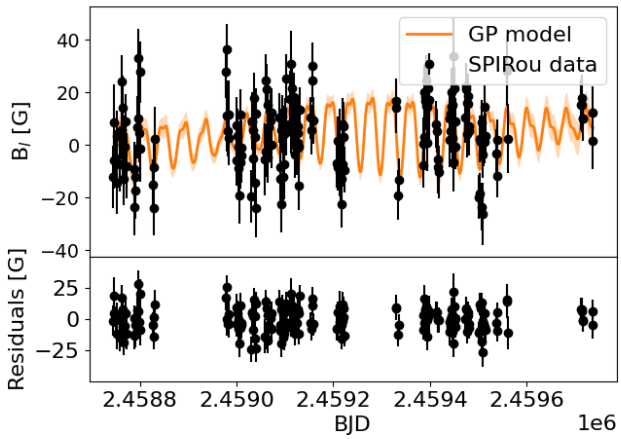


Fig. A.9. Same for GI 849.

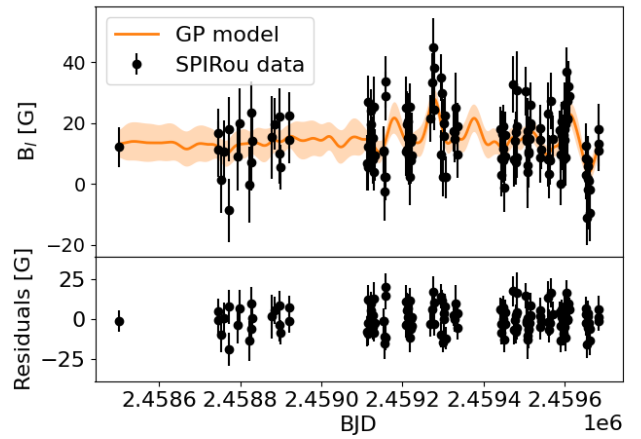


Fig. A.12. Same for GI 251 (five-parameter fit).

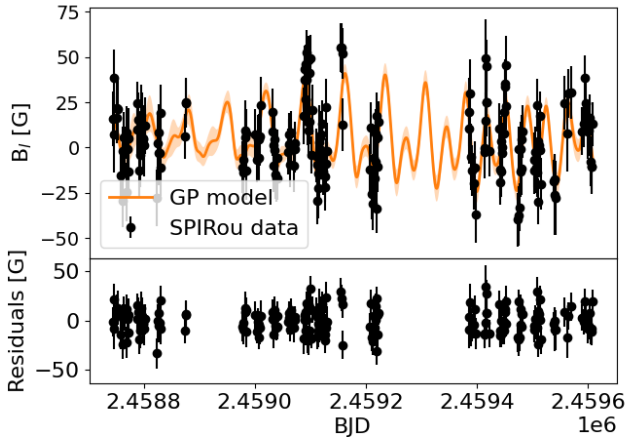


Fig. A.13. Same for GJ 4333.

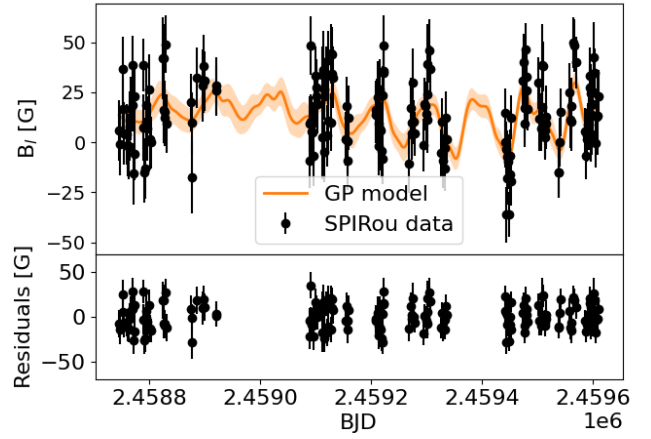


Fig. A.16. Same for GJ 3378.

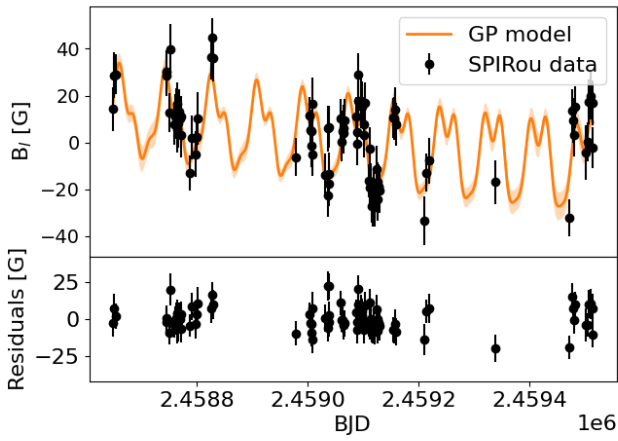


Fig. A.14. Same for GI 876.

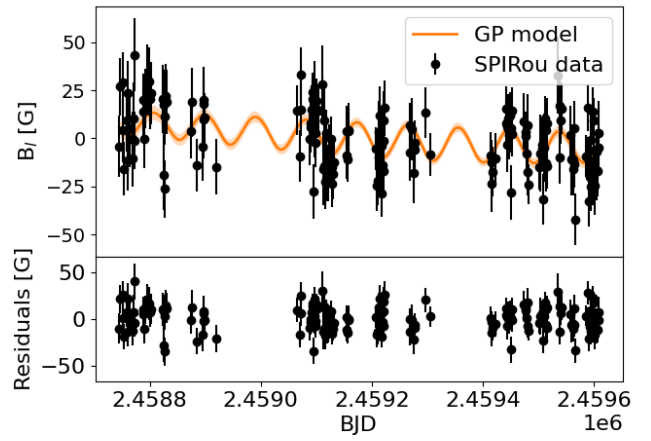


Fig. A.17. Same for GI 169.1A.

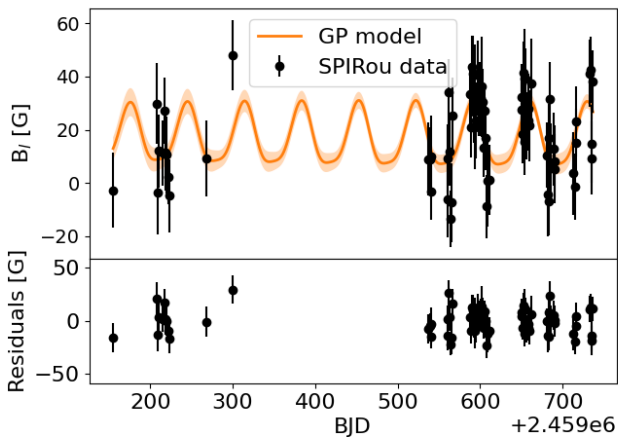


Fig. A.15. Same for PMJ09553-2715.

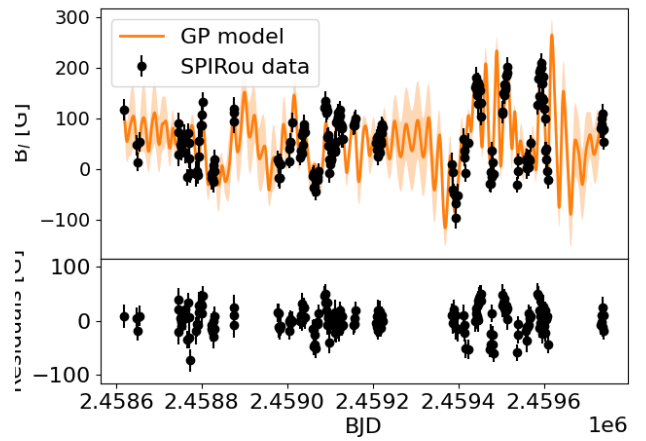


Fig. A.18. Same for GJ 1289.

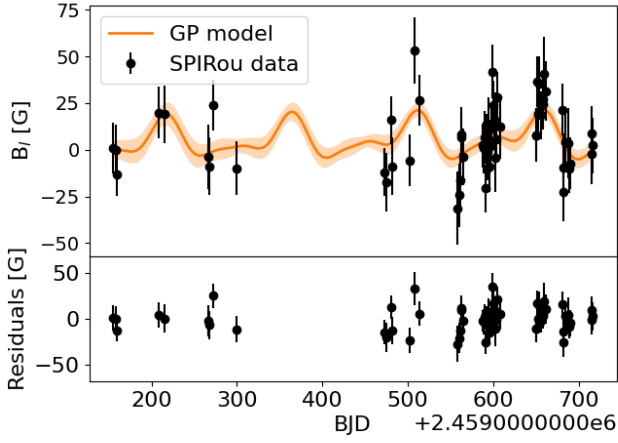


Fig. A.19. Same for GJ 1103 (five-parameter fit).

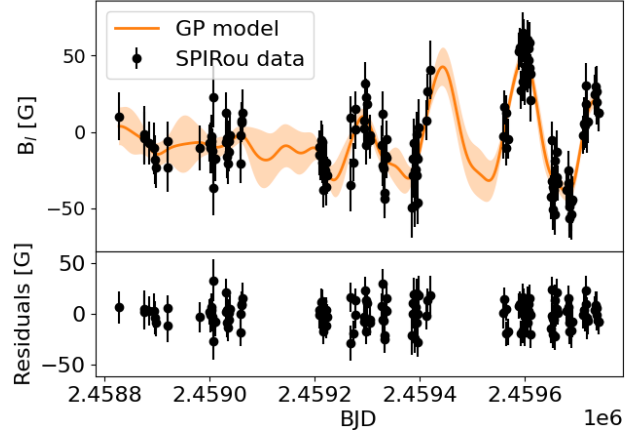


Fig. A.22. Same for GJ 1151 (five-parameter fit).

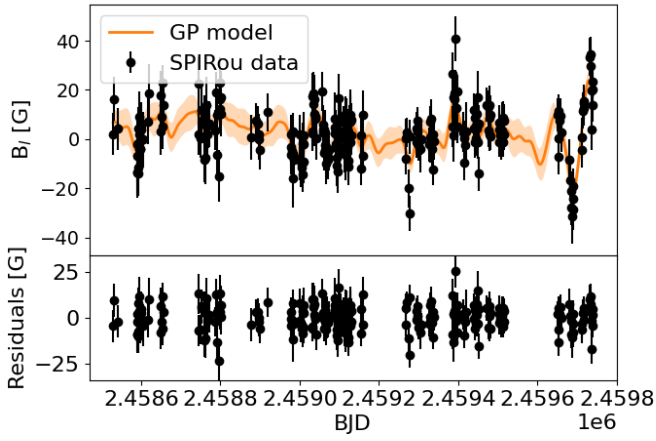


Fig. A.20. Same for GJ 699 (five-parameter fit).

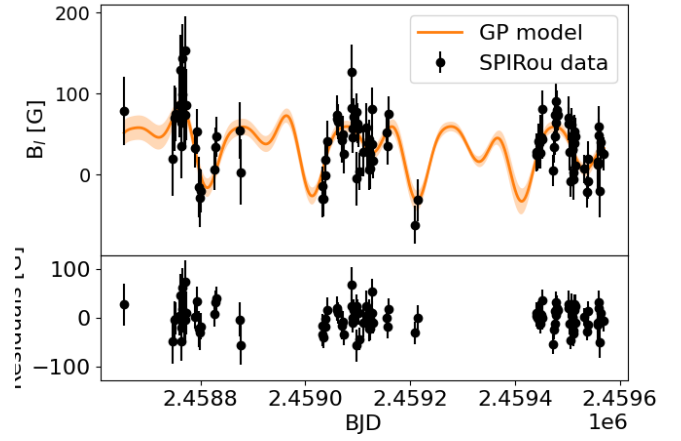


Fig. A.23. Same for GJ 1286 (five-parameter fit).

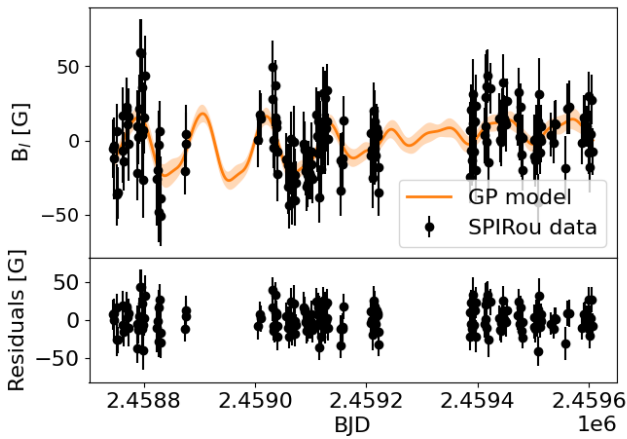


Fig. A.21. Same for GJ 15B (five-parameter fit).

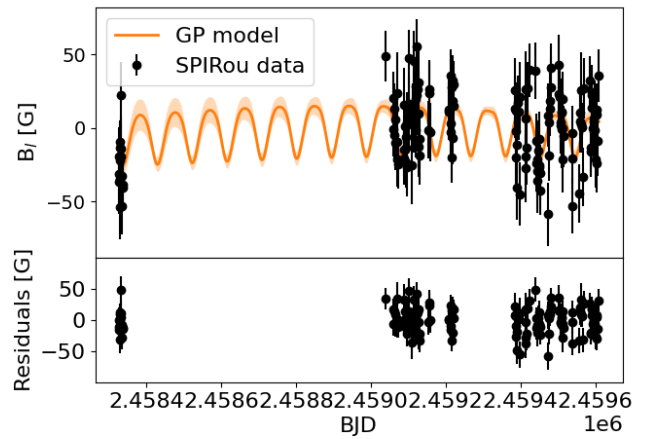


Fig. A.24. Same for GJ 1002.

Appendix B: Quasi-periodic Gaussian process regression for Gl 411

In this appendix, we study the particular case of the very long stellar rotation period measured for Gl 411 (460 days). We display the temporal evolution of the longitudinal magnetic field and its GP fit (Fig. B.1). We then display the associated corner plot showing the posterior distributions of each parameter (Fig. B.3).

At the suggestion of the referee, we compared the GP fit to a similar GP fit to reshuffled data. We kept the same observation dates, but attributed the B_ℓ measurements and their associated uncertainty randomly to a given date. The GP fit is now flat and shows that the detected periodicity in the actually measured data is real (Fig. B.2). We also display the associated corner plot for comparison. No periodic behavior can be detected at all (Fig. B.4).

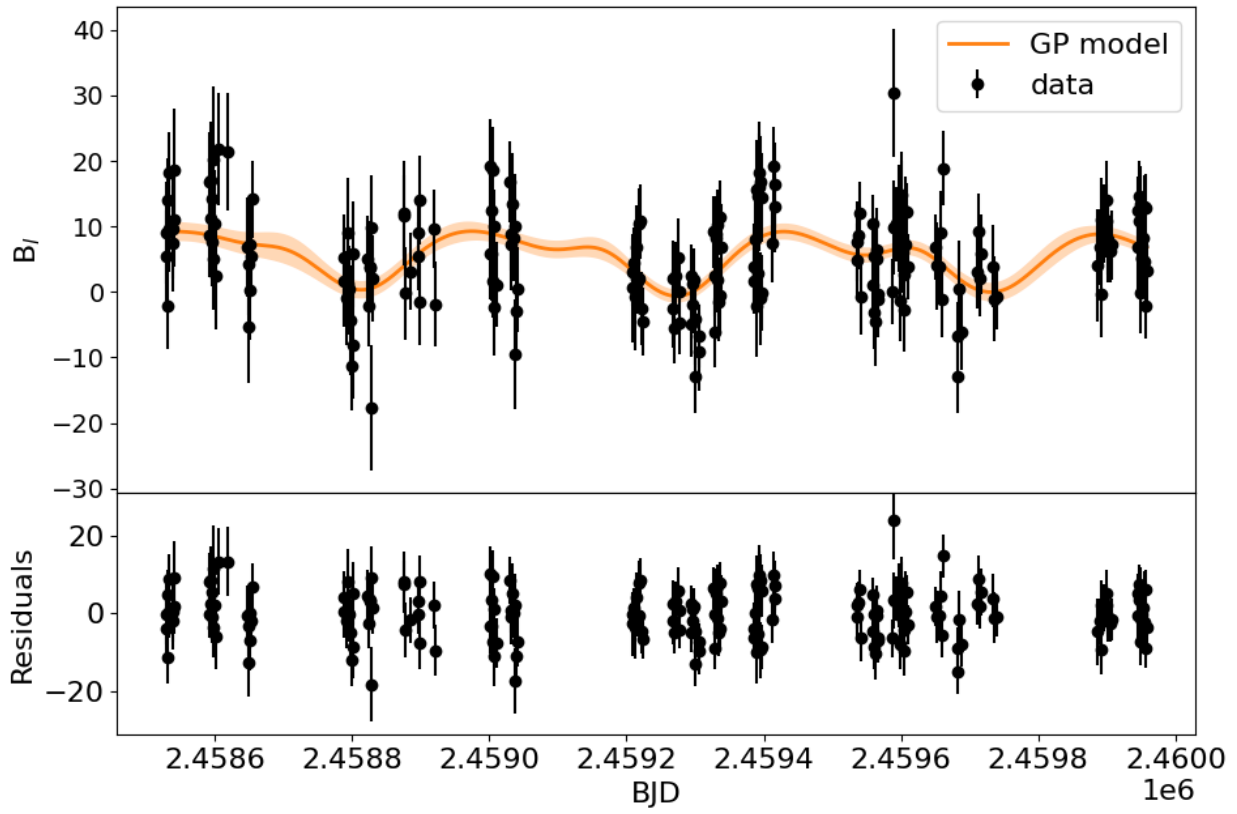


Fig. B.1. GP analysis of the SPIRou B_ℓ data of G1411. The top panel shows the observed B_ℓ data (black points) and the orange line shows the best-fit quasi-periodic GP model. The bottom panel shows the residuals of the six-parameter GP fit.

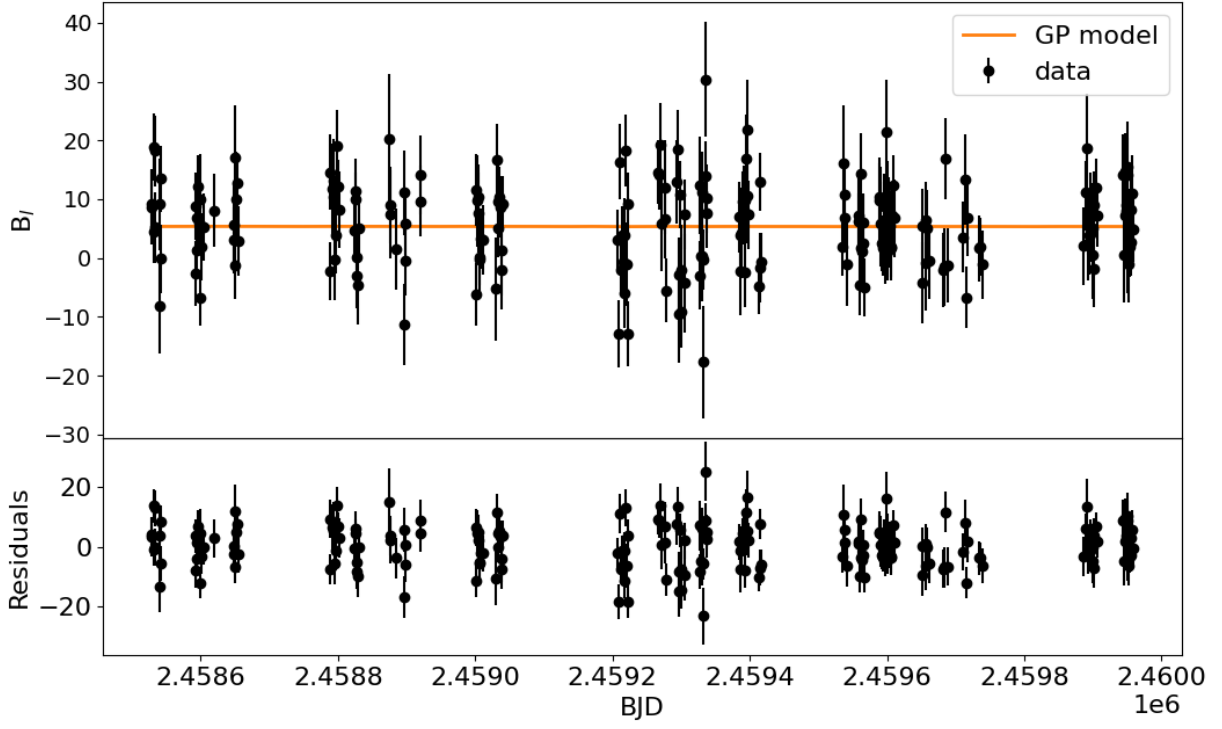


Fig. B.2. GP analysis of reshuffled B_ℓ data at the same observation dates as G1411.

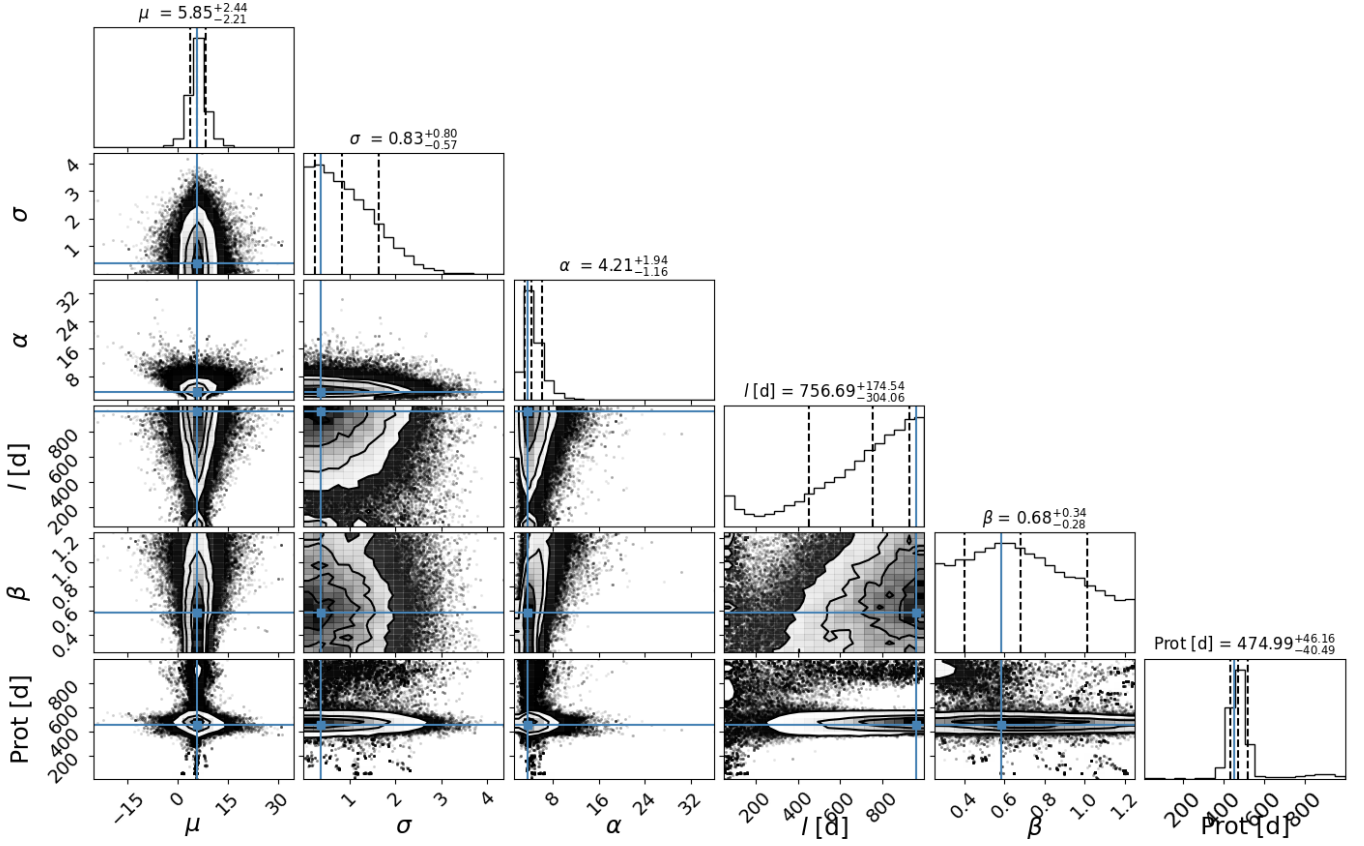


Fig. B.3. Corner plot of the posterior distribution of parameters of the GP fit for G1411.

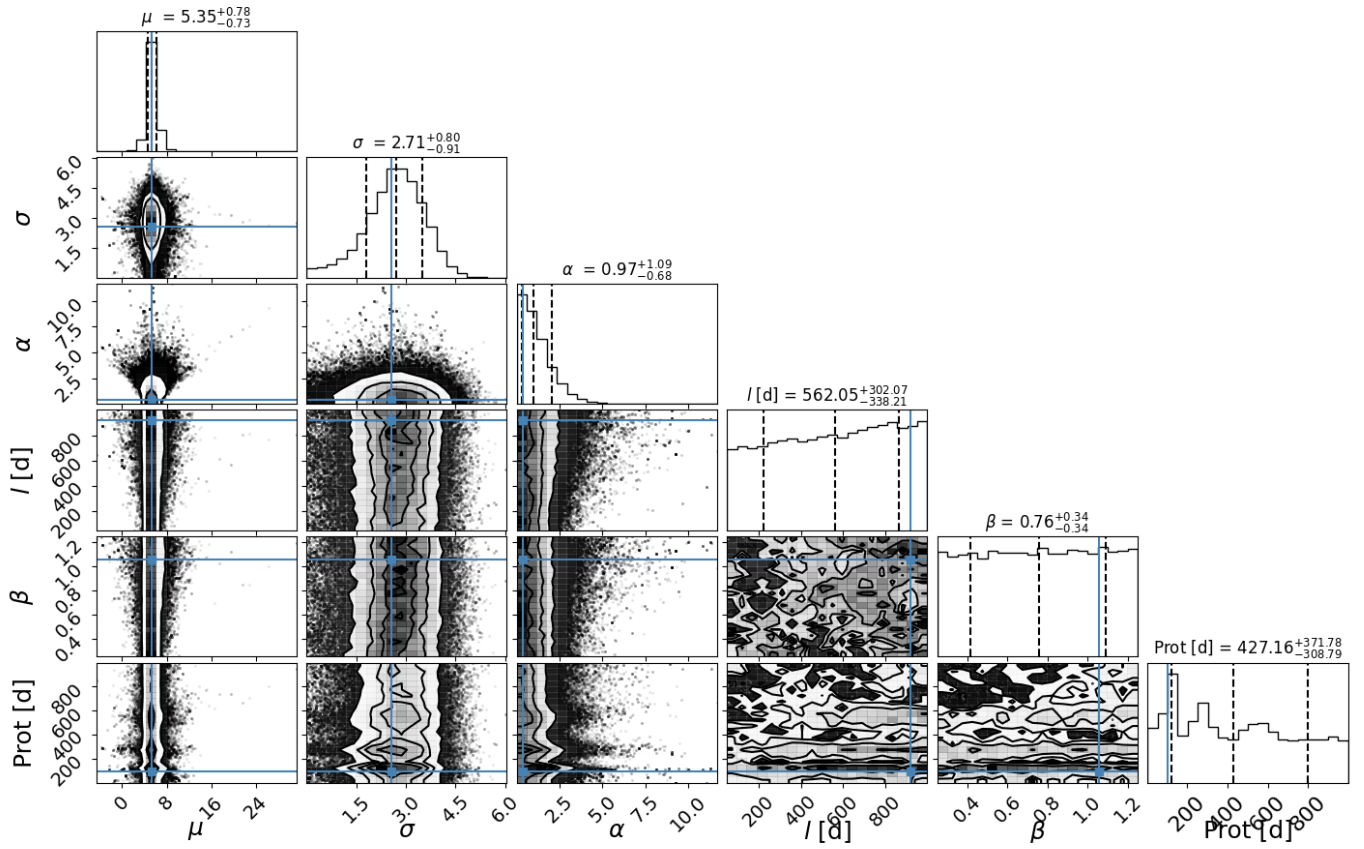


Fig. B.4. Corner plot of the posterior distribution of parameters of the GP fit for the reshuffled data at the observation dates of Gl 411.

Appendix C: Stokes V profiles of stars without a detected rotation period

We display here the temporal evolution of the Stokes V for the 16 stars of our sample (Figs. C.1 to C.16) for which we could not detect a periodic variation of the longitudinal magnetic field. This shows that for some stars, the Stokes V is well detected, but is constant or does not vary periodically, while for others, it is barely detected or not detected at all.

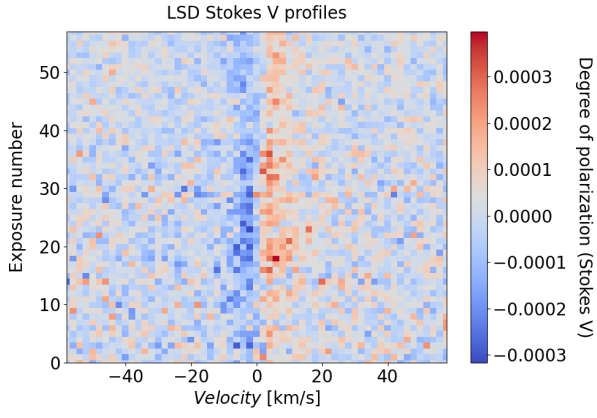


Fig. C.1. Temporal variation in Stokes V profiles of the SPIRou polarimetric series of G1338B.

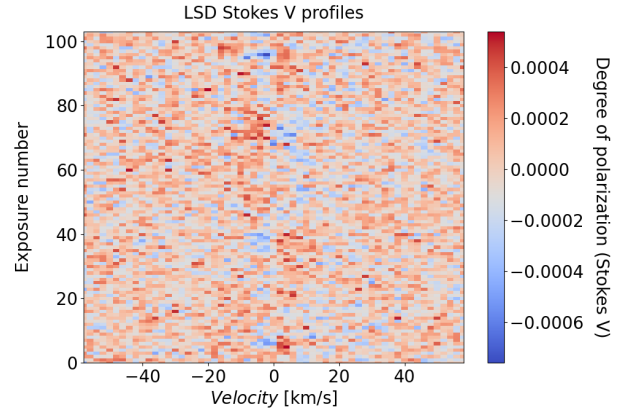


Fig. C.4. Same for G1480.

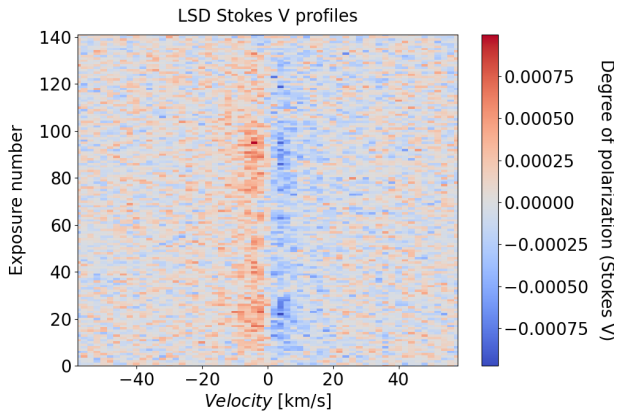


Fig. C.2. Same for G1617B.

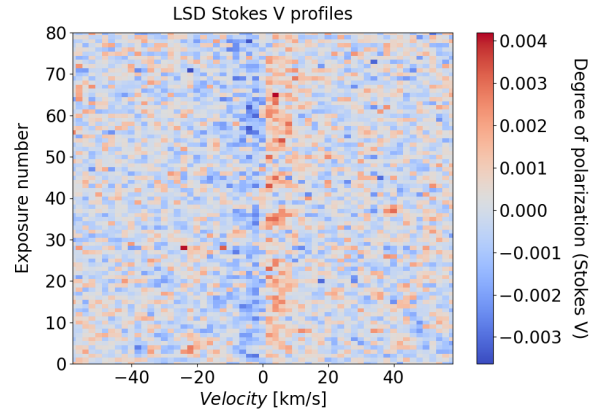


Fig. C.5. Same for G1436.

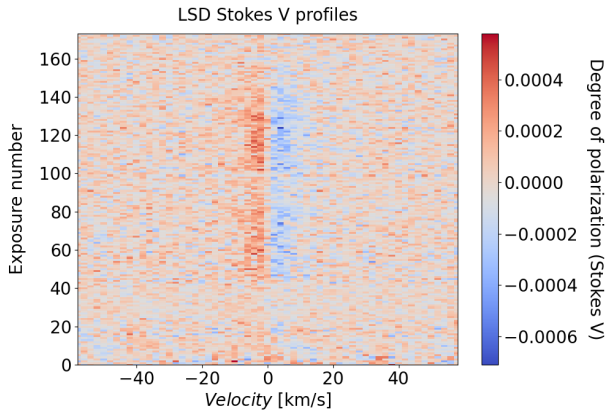


Fig. C.3. Same for G1412A.

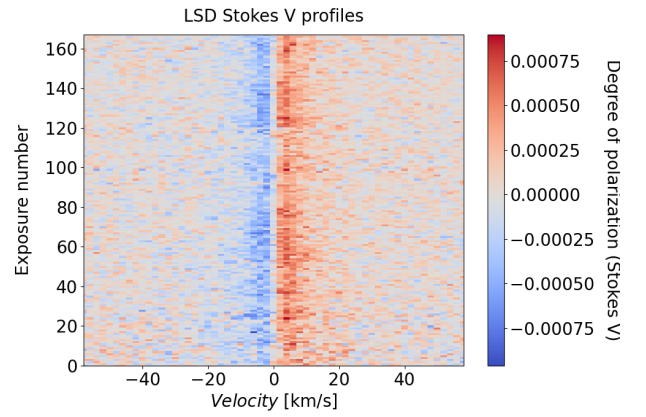


Fig. C.6. Same for G1408.

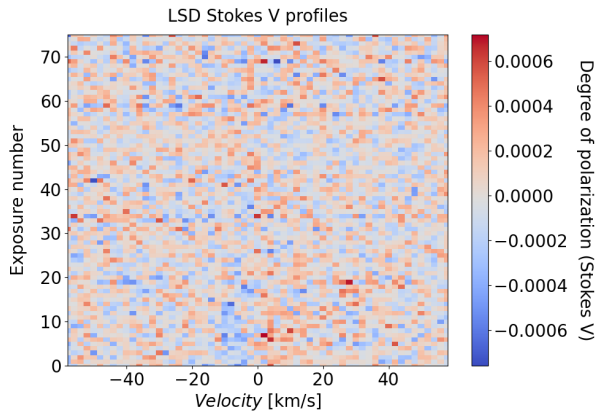


Fig. C.7. Same for GJ 1317.

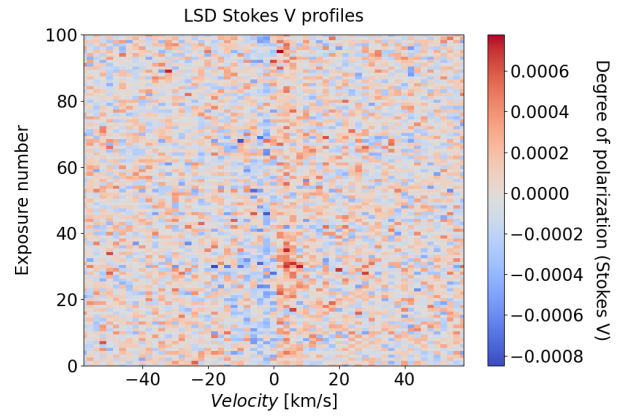


Fig. C.10. Same for GJ 1148.

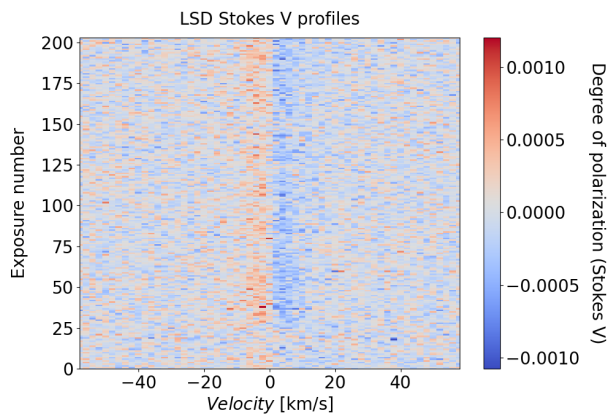


Fig. C.8. Same for GJ 4063.

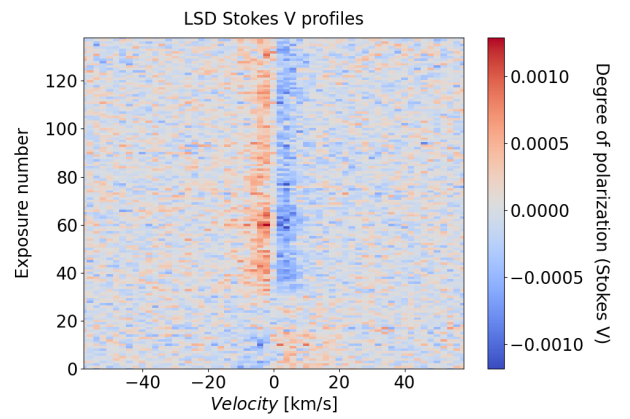


Fig. C.11. Same for PM J08402+3127.

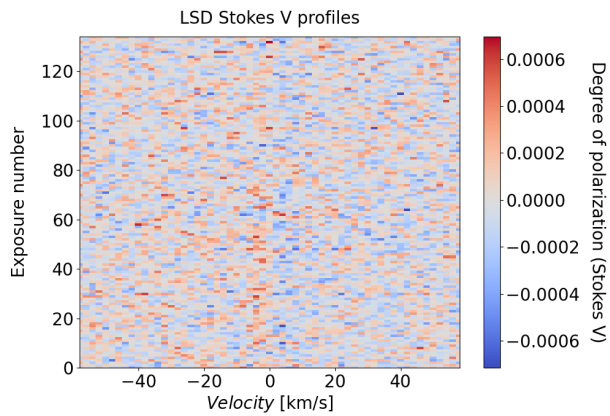


Fig. C.9. Same for GJ 1012.

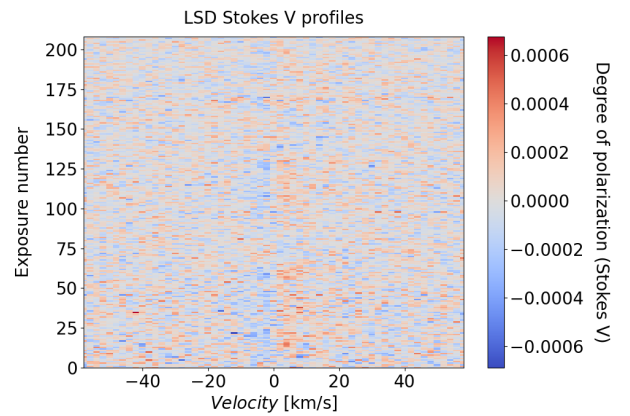


Fig. C.12. Same for GJ 725B.

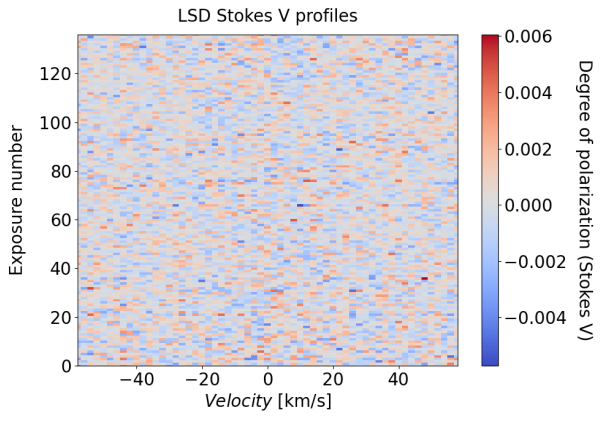


Fig. C.13. Same for GJ 1105.

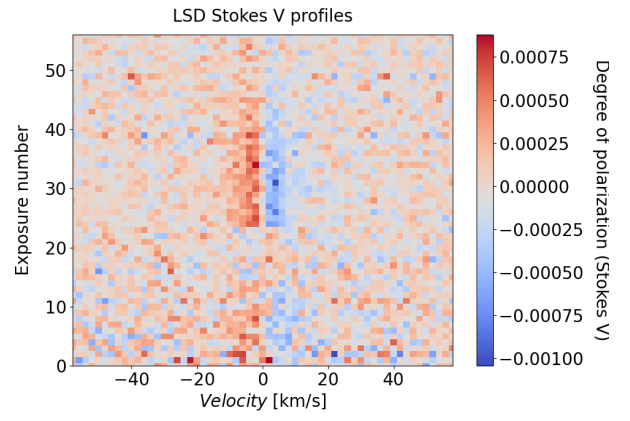


Fig. C.16. Same for Gl 447.

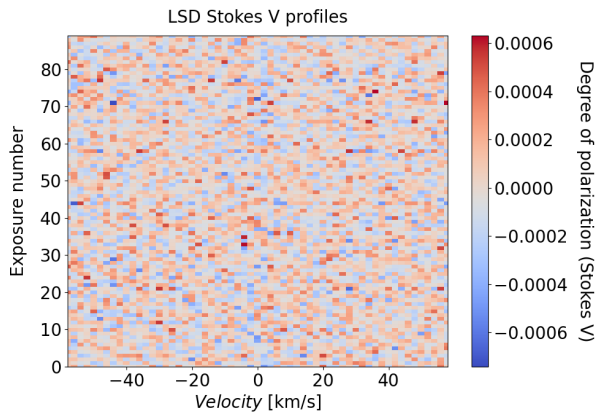


Fig. C.14. Same for Gl 445.

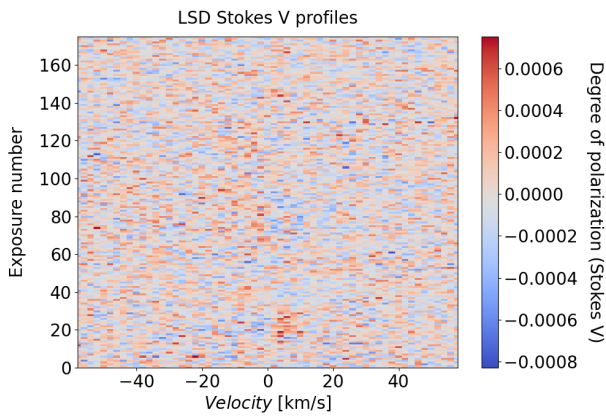


Fig. C.15. Same for PM J21463+3813.